

Cluster Difference Imaging Photometric Survey (CDIPS) II. TOI837: A Validated Jupiter-Sized Planet in IC 2602

L. G. BOUMA,¹ J. D. HARTMAN,¹ P. SARKIS,² P. EVANS,³ K. A. COLLINS,⁴ G. ZHOU,⁴ S. N. QUINN,⁴ J. DE LEON,⁵ J. LIVINGSTON,⁵ C. BERGMANN,⁶ K. G. STASSUN,^{7,8} C. G. TINNEY,^{6,9} W. BHATTI,¹ J. N. WINN,¹ G. Á. BAKOS,¹ T. HENNING,² R. BRAHM,^{10,11} N. ESPINOZA,¹² A. JORDÁN,^{10,11} M. BARBIERI,¹³ S. NANDAKUMAR,¹³ T. TRIFONOV,² J. VINES,¹⁴ M. VUCKOVIC,¹⁵ C. ZIEGLER,¹⁶ C. BRICEÑO,¹⁷ N. LAW,¹⁸ A. W. MANN,¹⁸ G. R. RICKER,¹⁹ R. VANDERSPEK,¹⁹ D. W. LATHAM,⁴ S. SEAGER,²⁰ J. M. JENKINS,²¹
ASTEP400 COLLABORATION, AND TSO/SPOC/POC REPRESENTATIVES

(Received July 6, 2020; Revised —; Accepted —)

Submitted to AAS journals.

ABSTRACT

We report the discovery of TOI 837.01 and its validation as a transiting planet. We characterize the system using data from the NASA TESS mission, the ESA Gaia mission, ground-based photometry, and spectroscopy from CHIRON, FEROS, and Veloce. We find that TOI837 is a $T = 9.9$ G0 dwarf in the open cluster IC 2602. The star and validated planet are therefore between 30 and 46 million years old. The planet is warm ($P = 8.32$ d) and roughly Jupiter-sized. Its transits are grazing: $b > 0.92$ at 3σ . From TESS photometry alone, the planetary size lies within $0.68\text{--}8.24 R_{\text{Jup}}$ ($3^{\text{rd}}\text{--}97^{\text{th}}$ percentile), due to the degeneracy between the planetary size and the impact parameter of the transit. From radial velocity monitoring, we limit the minimum mass to less than $1.20 M_{\text{Jup}}$ (3σ). Grazing transits are a cause for concern, as they are usually indicative of astrophysical false positive scenarios. Our follow-up data show that such scenarios are highly unlikely. Our combined multi-color photometry, high-resolution imaging, and radial velocities rule out hierarchical eclipsing binary scenarios. Background eclipsing binary scenarios, though limited by speckle imaging, formally remain a 0.2% possibility. TOI 837.01 is therefore a validated adolescent exoplanet. Further observations of its stellar obliquity, atmosphere, and mass should confirm its planetary nature beyond doubt, and could improve our understanding of how the physical and orbital properties of exoplanets change in time.

Keywords: Exoplanets (498), Transits (1711), Exoplanet evolution (491), Stellar ages (1581), Young star clusters (1833)

1. INTRODUCTION

Over the first 100 million years of their lives, exoplanet systems are expected to undergo major physical and dynamical changes. For a typical Sun-like star, the protoplanetary disk disperses within roughly 1–10 million years (Mamajek 2009; Dullemond & Monnier 2010; Williams & Cieza 2011). Gas giants presumably finish accreting before the end of disk dispersal (Pollack et al. 1996). While rocky planets may fully form within only a few million years (Dauphas & Pourmand 2011), they can also undergo significant changes over the next $\sim 10\text{--}100$ million years through giant impacts (e.g., Kleine et al. 2009; König et al. 2011; Raymond et al. 2014). The Moon, for instance, may have formed from debris ejected during a collision between the proto-Earth and a planetesimal during Earth’s first 100 million years (Cameron & Ward 1976; Canup & Asphaug 2001).

A number of other processes are expected to shape young exoplanets. Planets with gaseous envelopes are thought to shrink as they contract and as their atmospheres undergo photoevaporation (e.g., Fortney et al. 2007; Owen & Wu 2013; Fulton et al. 2017). The relative importance of contraction and photoevaporation is set by the planetary mass, as well as the radiation environment. The effectiveness of photoevaporation can be inferred from observations of planetary winds in the metastable 1083 nm He line (Spake et al. 2018; Oklopčić & Hirata 2018; Mansfield et al. 2018).

Beyond physical changes, dynamical changes are expected in the semi-major axes, eccentricities, and stellar obliquities of young planets. When the gas disk is present, the planetary semi-major axis is thought to change in step with the viscous evolution of the disk (Lin et al. 1996). High-eccentricity migration processes including planet-planet scattering, secular chaos, and Kozai-Lidov oscillations can also occur (e.g., Chatterjee et al. 2008; Lithwick & Wu 2014; Fabrycky & Tremaine 2007). The circularization timescale is thought to be such that for any giant planets that migrated early, their orbits should circularize within 100 million years (Zahn 1977).

Finding and studying systems undergoing these evolutionary changes is a major goal in contemporary exoplanet research. To identify stars younger than say 1 Gyr, a number of direct and indirect methods are available (Soderblom 2010). The traditional approach is to isochronally age-date coeval groups of stars, hereafter “clusters” (e.g., Lada & Lada 2003; Zuckerman & Song 2004; Krumholz et al. 2019). Young field stars can also be identified using age indicators such as stellar rotation periods, the abundance of photospheric lithium, and chromospheric diagnostics such as calcium emission and broadband UV emission. Studies by for instance David et al. (2018) and G. Zhou et al. (2020, submitted) have combined these methods for individual field stars. Many of the latter methods were summarized by Mamajek & Hillenbrand (2008), and have since been calibrated by e.g., Irwin & Bouvier (2009); Barnes et al. (2015); Meibom et al. (2015); Angus et al. (2015) and Curtis et al. (2019b) for stellar rotation, Žerjal et al. (2017) for chromospheric activity, and e.g., Eliott et al. (2016); Berger et al. (2018) and Žerjal et al. (2019) for lithium abundances.

A few dozen planets in clusters have been detected, and fewer still have been closely characterized. Despite the challenges of starspot-induced radial velocity (RV) variations, RV surveys found success in the Hyades, NGC 2523, Praesepe, and M 67 (Sato et al. 2007; Lovis & Mayor 2007; Quinn et al. 2012; Malavolta et al. 2016; Brucalassi et al. 2017). RV surveys of highly active pre-main sequence stars in Taurus also led to the youngest hot Jupiters yet reported (Donati et al. 2016; Johns-Krull et al. 2016; Biddle et al. 2018; Flagg et al. 2019).

The transit method was comparatively slow to catch up. Early deep transit searches of open clusters by many groups did not yield definitive planet detections (Mochejska et al. 2005, 2006; Burke et al. 2006; Aigrain et al. 2007; Irwin et al. 2007; Miller et al. 2008; Pepper et al. 2008; Hartman et al. 2009). These searches were typically sensitive to planets larger than Jupiter, on $\lesssim 3$ day orbital periods. Hot Jupiter occurrence rate limits were derived at the $\lesssim 5\%$ level (e.g., Burke et al. 2006; Hartman et al. 2009). The modern 0.5–1% occurrence rate suggests that these early transit surveys needed a greater data volume, at higher precision for detection to be possible (Mayor et al. 2011; Wright et al. 2012; Howard et al. 2012; Petigura et al. 2018).

Kepler observed a large enough number of stars with sufficient baseline and precision to detect transiting planets in open clusters: Kepler-66b and 67b, in the gigayear-old NGC 6811 (Borucki et al. 2010; Meibom et al. 2013). Though a broken reaction wheel ended the prime Kepler mission, the repurposed K2 (Howell et al. 2014) switched between fields along the ecliptic every quarter-year, and was able to observe far more clusters and young stars.

The discoveries made by K2 through its surveys of Taurus, the Hyades, Praesepe, and Upper Sco were a major inspiration for the present work (e.g., Mann et al. 2016a; Obermeier et al. 2016; Mann et al. 2017; Vanderburg et al. 2018; Ciardi et al. 2018; Livingston et al. 2018; Mann et al. 2018; Rizzuto et al. 2018; Livingston et al. 2019). Observations with K2

convincingly showed that at least some close-in planets must form within about 10 Myr (Mann et al. 2016b; David et al. 2016). They also led to the first hints that young planets may in fact be qualitatively different from their field counterparts. For instance, based on its observed mass, radius, and UV environment, the 700 Myr K2-100b is probably actively losing its atmosphere, and should become a bare rocky planet over the next few hundred Myr (Mann et al. 2017; Barragán et al. 2019). The four transiting planets in V1298 Tau (23 Myr) are also likely to be actively photoevaporating, and could represent a precursor to Kepler’s compact multiple systems (David et al. 2019a,b).

With the aim of advancing the young planet census, we have been using data from the TESS spacecraft (Ricker et al. 2015) to perform a Cluster Difference Imaging Photometric Survey (CDIPS; Bouma et al. 2019). Our targets in this survey are candidate young stars that have been reported in the literature. At the time writing, of order 6×10^5 light curves from the first year of TESS observations have been reduced, and are available at MAST¹ through DOI.ORG/10.17909/T9-AYD0-K727. Searching these light curves yielded the candidate transiting planet, TOI 837.01, that is the subject of this analysis.

The transits of TOI 837.01 are grazing, which is a cause for concern. Particularly for a target near the galactic plane ($b = -5.8^\circ$), background eclipsing binaries are a major source of astrophysical false positives (e.g., Sullivan et al. 2015, Figure 30). Our follow-up data show that this and related scenarios are unlikely to the degree that we can “validate” the planet, *i.e.*, rule that its probability of being an astrophysical false positive is negligibly small. We considered this result worth reporting because of the planet’s youth.

Section 2 describes the identification of the candidate, and the follow-up observations collected. Section 3 combines these data to assess the system’s false positive probability, and validates TOI 837.01 as a planet. Section 4 presents our knowledge of the cluster (Section 4.1), the star (Section 4.2) and the planet (Section 4.3). We conclude by discussing avenues for confirmation and improved characterization in Section 5.

2. IDENTIFICATION AND FOLLOW-UP OBSERVATIONS

2.1. TESS Photometry

TOI 837 was observed by TESS from 26 March 2019 until 20 May 2019, during the tenth and eleventh sectors of science operations (Ricker et al. 2015). The star was designated TIC 460205581 in the TESS Input Catalog (Stassun et al. 2018, 2019). Pixel data for an 11×11 array surrounding the star were averaged and saved at 2-minute cadence. The 2048×2048 image from the entire CCD was also averaged into 30-minute stacks, and saved as a “full frame image” (FFI).

¹ ARCHIVE.STSCI.EDU/HLSP/CDIPS

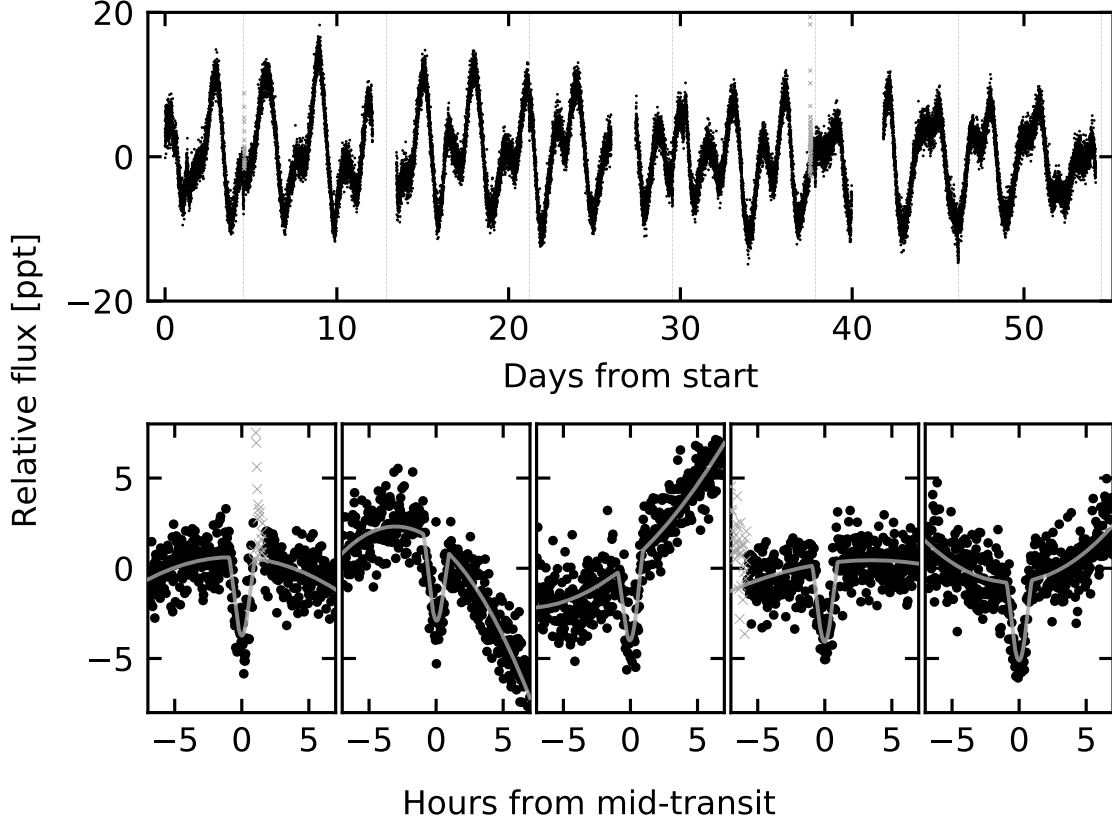


Figure 1. TESS light curve of TOI 837 from Sectors 10 and 11. *Top:* PDCSAP median-subtracted relative flux at 2-minute sampling in units of parts-per-thousand ($\times 10^{-3}$). Starspot-induced variability is the dominant signal; flares are shown with gray crosses. Dashed lines indicate the five transits observed by TESS. *Bottom:* Zoomed windows of individual transits. Gray lines are the best-fit transit model, which includes a local quadratic trend in each window.

The TESS project detected the transits in the 2-minute data and the community was alerted on 17 June 2019. While our CDIPS FFI light curves also showed the transits, the 2-minute data had better sampling cadence, and so we opted to use the Presearch Data Conditioning (PDC) light curve with the default aperture for our analysis (Smith et al. 2012; Stumpe et al. 2014; Jenkins et al. 2016; Smith et al. 2016).

Figure 1 shows the data. The dominant modulation induced by starspots coming into and out of view has a peak-to-peak amplitude of about 2.3%, and a period of about 3 days. The dips suggestive of a grazing transiting planet recur roughly every 8 days, and have a depth of about 0.4%. A few flares are visible. A phase-folded view of the TESS transits with starspot variability removed is shown in Figure 2. Our fitting procedure for the models shown in these plots is described in Section 4.3.

2.2. Gaia Astrometry and Imaging

Between 25 July 2014 and 23 May 2016, the ESA Gaia satellite measured about 300 billion centroid positions of 1.6 billion stars. The positions, proper motions, and parallaxes of the brightest 1.3 billion were calculated for the second data release (DR2) (Gaia Collaboration et al. 2016; Lindegren et al. 2018; Gaia Collaboration et al. 2018). TOI 837 was as-

signed the Gaia DR2 identifier 5251470948229949568, and had 276 “good” astrometric observations. Its brightness was measured in the G , R_p , and B_p bands of the Radial Velocity Spectrometer (Cropper et al. 2018; Evans et al. 2018).

The Gaia imaging, reduced to its point-source catalog, provides the initial context for analyzing the TESS data. Stars brighter than $T = 16$, as queried from the Gaia DR2 source catalog, are shown with white circles in Figure 3, overlaid on the DSS2 plates and TESS image. Given its galactic latitude of $b = -6^\circ$, it is not surprising that the field of TOI 837 is crowded. The resolved stars that were of immediate concern for our false positive analysis were as follows.

- TOI 837 \equiv TIC 460205581 ($T = 9.9$). The target star.
- Star A \equiv TIC 847769574 ($T = 14.6$), $2.3''$ west. The proper motions and parallax of this star imply it is co-moving with TOI 837, though with a physical separation of 6.6 ± 0.1 pc, it may not be bound.
- Star B \equiv TIC 460205587 ($T = 13.1$), $5.4''$ north. The Gaia parallax implies this is a giant background star.

An additional source, TIC 847769581, is $4.9''$ from the target, but too faint ($T = 18.8$) to be the source of the observed transit signal.

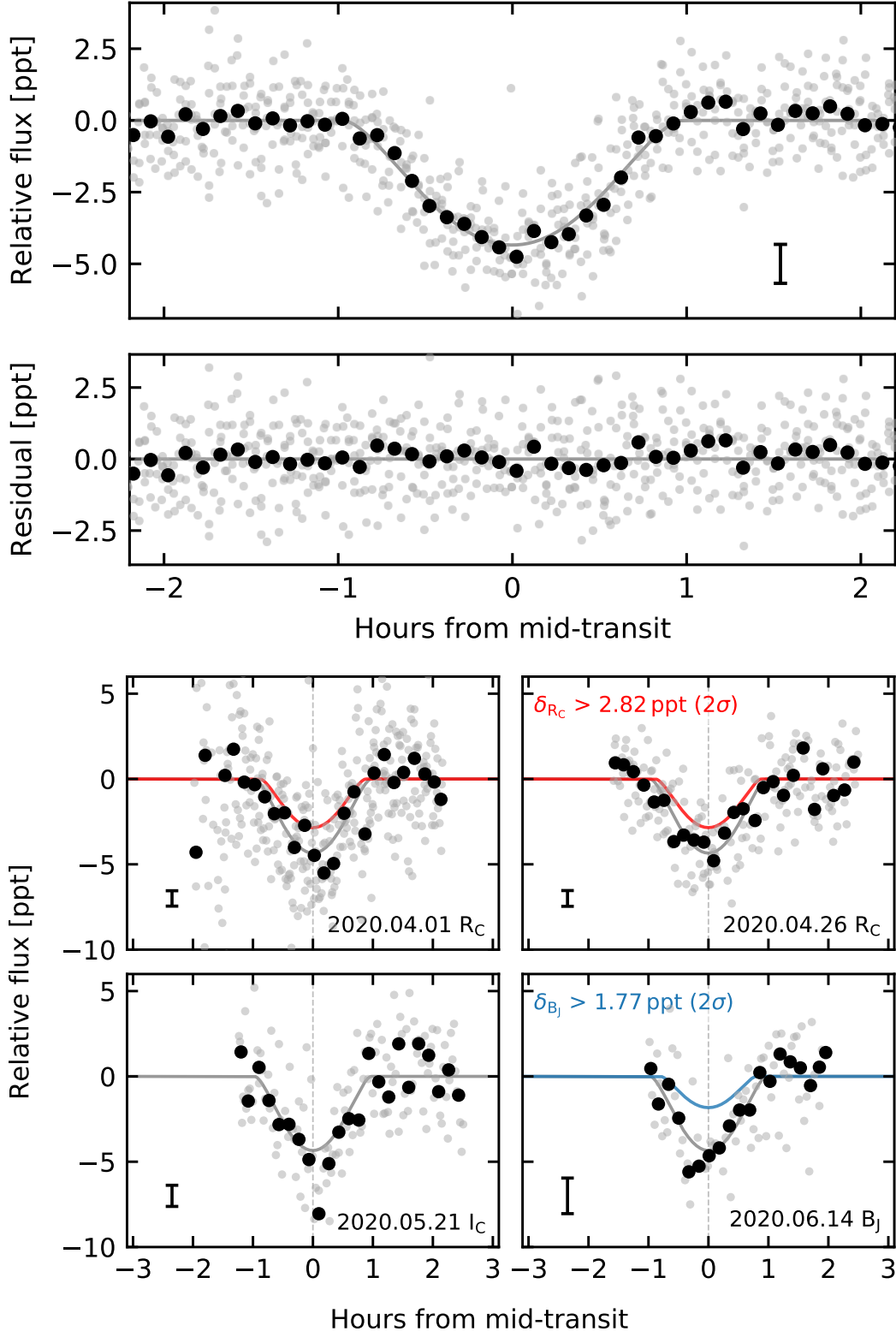


Figure 2. Photometry of TOI 837. *Top:* Phase-folded TESS transit. Gray points are 2-minute PDCSAP flux measurements with the local spot-induced variation removed. Black points are binned to 6-minute intervals. The black error-bar shows the median uncertainty for the black points. The gray line is the best-fit model to the combined TESS and ground-based data (Table 3). *Bottom:* Multicolor photometry from the El Sauce 0.36m; black points are binned to 10-minute intervals. Models show 2σ lower limits on the transit depths in the Cousins-R and Johnson-B bandpasses used to rule out specific false positive scenarios (see Section 3.1.5).

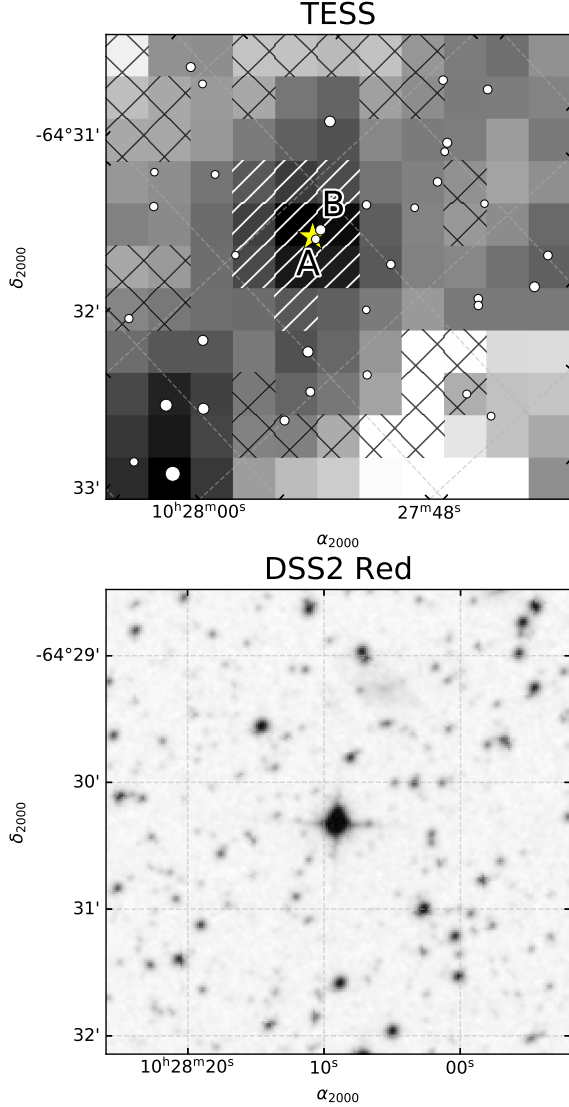


Figure 3. Scene of TOI 837. *Top:* Mean TESS image of TOI 837 over Sector 10, with a logarithmic grayscale. The yellow star is the position of TOI 837. White circles are neighboring stars with $T < 16$ (brighter stars are larger). The black X and white / hatches show the apertures used to measure the background and target star flux, respectively. Dashed lines of constant declination and right ascension are shown. *Bottom:* Digitized Sky Survey R -band image of the same field, with a linear grayscale. Two stars of interest are “Star A” and “Star B”, which were eventually excluded as being possible sources of the transits.

The Gaia DR2 data for Star A seems poorly behaved. While Star A has $G = 15.1$, and $Bp = 14.9$, no Rp magnitude is reported. Correspondingly, no RUWE² value is available. We suspect that the photometric failure to produce an

Rp magnitude, as well as its poor astrometric fit, are likely due to blending with TOI 837.

At the $\approx 1'$ resolution of the TESS data, if either Star A or Star B were eclipsing binaries, they could be the sources of the transit signal. A detailed analysis of ground-based seeing-limited photometry was necessary to assess and rule out this possibility (Section 2.4).

2.3. High-Resolution Imaging

To determine if any fainter point sources existed closer to TOI 837 inside of Gaia’s point-source detection limits, we acquired high-resolution speckle images. We then searched the autocorrelation functions of these images for peaks indicative of nearby companions.

Carl TODO: please describe and correct as appropriate The observations of TOI 837 were initially acquired by Ziegler et al. (2020) as part of the Southern Astrophysical Research (SOAR) TESS Survey using the High Resolution Camera (HRCam; Tokovinin 2018). The HRCam I -band filter is described by Tokovinin (2018). The points in Figure 4 show the resulting measured $5\text{-}\sigma$ detectable contrasts. The lines are linear smoothing fits between the regimes of the diffraction limit, the “knee” at $\approx 0.2''$, and the slow decrease until $\approx 1.5''$, beyond which the speckle patterns become de-correlated. Star A (TIC 847769574) was detected at the expected location and brightness contrast, and no additional companions were found. Star B was not detected; with a separation of $5.4''$ from TOI 837, it fell outside the field of view.

2.4. Ground-based Time-Series Photometric Follow-up

We obtained ground-based seeing-limited time series photometric observations of TOI 837 bracketed around the times of transit. These observations confirmed that the transits occurred on-target to within $\approx 2''$, and that they were achromatic. Both features are essential for our ability to eliminate false-positive scenarios.

2.4.1. El Sauce 0.36m

Acquisition and reduction—We observed four transits with the 0.36m at Observatorio El Sauce, located in the Río Hurtado Valley in Chile, and operated by co-author P. Evans. The observations were obtained in Cousins-R band on the nights of 1 April 2020 and 26 April 2020, Cousins-I band on the night of 21 May 2020, and Johnson-B band on the night of 14 June 2020. The final 14 June transit began shortly after twilight.

Phil + Karen TODO: please correct as appropriate We scheduled the observations using **SOFTWARE** (CITE). The photometric data were calibrated and extracted using the *AstroImageJ* software package (Collins et al. 2017). Comparison stars of similar brightness were used to produce the final light curves, each of which showed a roughly 4ppt dip near the expected transit time.

Custom aperture analysis—Based solely on the TESS data, both Star A and Star B were possible sources of blended

² See the Gaia DPAC technical note GAIA-C3-TN-LU-LL-124-01, http://www.rssd.esa.int/doc_fetch.php?id=3757412, accessed 2020-06-22.

eclipsing binary signals. Star B is resolved in the ground-based images; Star A is not.

To rule out blend scenarios with the ground-based photometry, we produced light curves centered on TOI 837 with circular apertures of radii ranging from $0.7''$ to $5.1''$. We did not detect any statistically significant variation in the depth of the transits with aperture size. Two lines of evidence rule out Star B as the eclipsing source: first, the transits were detected in the smallest apertures. Second, we made light curves with $2.1''$ apertures centered on Star B, and they did not show the transit.

To assess the possibility that Star A is an eclipsing body, we created light curves with a custom set of circular apertures with radii of $2.1''$ and positions ranging from Star A ($2.3''$ west of TOI 837) to $2.3''$ east of TOI 837. We did not detect any variation of the transit depth along this line of light curves, as would be expected if Star A were the eclipse host. The apertures east of TOI 837 exclude over 90% of the flux from Star A. The eclipse on Star A would therefore need to be excessively deep to produce the observed eclipse depth. We take this as evidence that TOI 837 is the source of the transit signal to within $\approx 2.0''$.

2.4.2. ASTEP400

Amaury TODO: please correct as appropriate We observed N transits with the 0.40m ASTEP 400 telescope at Concordia Station, located at Dome C on the Antarctic Plateau (Daban et al. 2010). ASTEP 400 has a dichroic that sends blue wavelengths to a guiding camera, and red wavelengths to a filter-free science camera with wavelength sensitivity roughly akin to R band. The observations were acquired on the nights of **DATE 1** and **DATE 2**. The outdoor temperature was a balmy XX° . The data were reduced using **XX** software, and showed the transit roughly at the expected time and depth.

2.5. Spectroscopic Follow-up

Reconnaissance spectroscopic follow-up is an essential step in vetting planet candidates. Medium to high-resolution spectra enable physical characterization of the star and therefore planet. Reducing multiple spectra to a radial velocity time-series can enable planet mass measurements, and also set limits on the mass of any nearby companions. Finally, if there are close or bright companions, reconnaissance spectra can also reveal the presence of a secondary set of stellar lines.

2.5.1. SMARTS 1.5m / CHIRON

We acquired nine spectra using CHIRON at the SMARTS 1.5m telescope at Cerro Tollo Inter-American Observatory, Chile (Tokovinin et al. 2013). Six met our signal-to-noise requirements for radial velocity measurements and stellar parameter extraction. We used CHIRON in its image slicer configuration, yielding a spectral resolution of $\approx 79,000$ across 415–880nm.

George TODO: please describe the formal secondary line search in more depth in this paragraph We searched

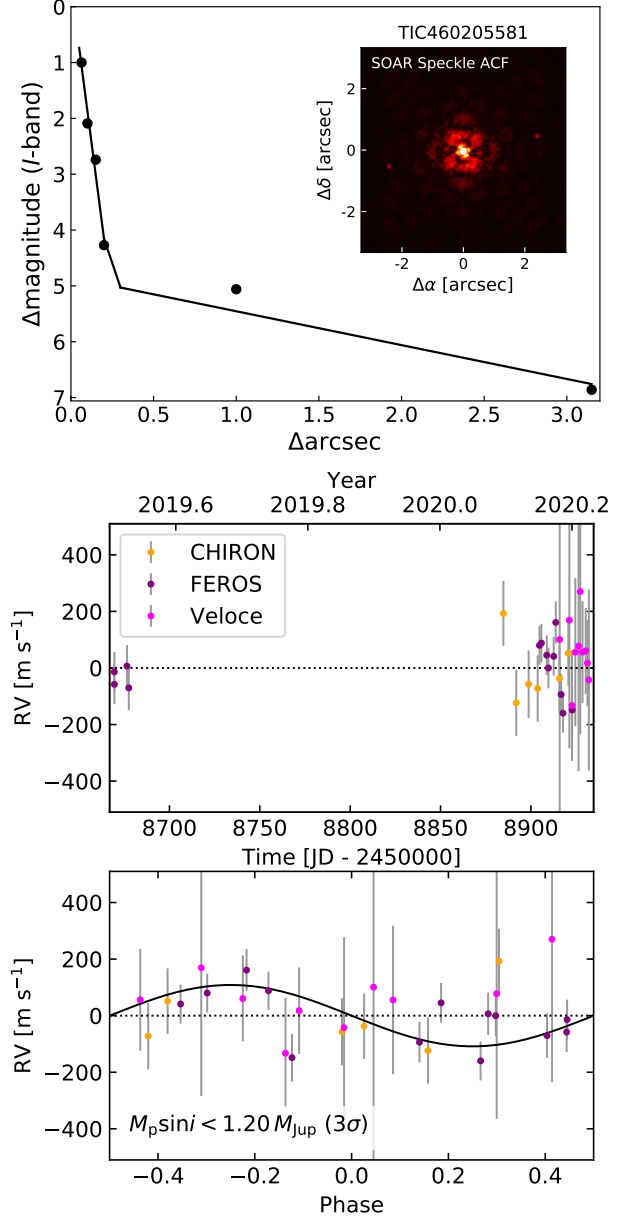


Figure 4. Following speckle-imaging and velocimetry of TOI 837. *Top:* SOAR HRCam contrast limits derived from point-source injection-recovery experiments. Star A ($\Delta T = 4.7$, $2.3''$ west) is detected in the autocorrelation function, and is also a resolved Gaia source. It is co-moving with TOI 837, and its parallax and on-sky position imply that it is physically separated from TOI 837 by 6.6 ± 0.1 pc. *Middle:* Radial velocity (RV) measurements, with best-fit instrument offsets and jitter terms included. The expected scatter from starspots based on $v \sin i$ and the photometric modulation amplitude is of order 300 m s^{-1} . *Bottom:* RV measurements phased to the orbital ephemeris of TOI 837.01. The planet is not detected. The black line shows a circular Keplerian orbit representing the 3σ upper mass limit.

for secondary lines in the CHIRON spectra by cross-correlating against a **template of some kind**. This rules out lines with flux ratios of $\approx 2\%$, if the lines are well-separated in velocity. To derive the star’s physical parameters, we cross-correlated the template against **something**, and used the **nameofcode**. We measured the radial velocities through a least-squares deconvolution of the observed spectra against the same synthetic template. The resulting velocities are given in Table 5, and shown in Figure 4.

2.5.2. FEROS

We acquired 13 spectra using the FEROS echelle spectrograph, mounted on the MPG 2.2m telescope at the European Southern Observatory in La Silla, Chile (Kaufer et al. 1999). FEROS has a resolution of $\approx 48,000$ across a spectra range of 350–920nm. It has a remarkably high efficiency of $\approx 20\%$.

We used the dedicated instrument pipeline to extract 1-dimensional, wavelength calibrated spectra. To measure radial velocities, **Rafael TODO: what procedure was used? What software packages?.** The velocities are given in Table 5, and shown in Figure 4.

2.5.3. Veloce

We acquired 34 spectra over 10 visits of TOI 837 with using the Veloce spectrograph, mounted on the AAT 4.0m telescope at Siding Spring Observatory near Coonabarabran, Australia (Gilbert et al. 2018). In Rosso form, Veloce provides coverage from 600–950nm at a spectral resolution of $\approx 80,000$.

Many of the exposures were taken in average or poor seeing conditions, when fiber-to-fiber cross-contamination on the IFU-style fiber feed is strongest. To reduce the spectra to velocities, we cross-correlated against a high S/N template of δ Pavonis. The velocity RMS seen across each visit was hundreds of meters per second, likely due to uncorrected fiber-to-fiber cross-contamination. For analysis purposes, we averaged across each visit, and set the velocity uncertainties to be the standard deviation of the per-visit exposures. The velocities are given in Table 5, and shown in Figure 4.

3. ELIMINATION OF FALSE POSITIVE SCENARIOS

Validating a transiting planet means statistically arguing that the data are much more likely to be explained by a planet than by an astrophysical false positive. The concept of validation has been developed and calibrated by *e.g.*, Torres et al. (2011); Morton (2012); Díaz et al. (2014); Santerne et al. (2015); Morton et al. (2016) and Giacalone & Dressing (2020). “Validation” is different from “confirmation”, which means that there is overwhelming evidence that the transits *must* be explained by a planet, through elimination of all false positive scenarios and determination that the planet’s mass is in the substellar regime.

Assuming an eclipse has been localized to the target star, potential false positive scenarios include eclipses of a background binary (BEB), eclipses of a hierarchical system bound to the primary star (HEB), and the possibility that the eclipses

are simply caused by a stellar companion, rather than a planetary one (EB).

Figure 5 provides a visual summary of the possible astrophysical false positive scenarios, as well as our ability to rule them out based on our combined photometry, velocimetry, and imaging. In this Section we describe each constraint in turn, and then present a calculation using VESPA (Morton 2012) to demonstrate that the probability TOI 837 is an astrophysical false positive is small enough to formally validate it as a planet.

3.1. Constraints on False Positive Scenarios

3.1.1. Transit Depth

In HEB and BEB scenarios, the flux from TOI 837 and the true eclipsing binary host blend together, and reduce the “true” eclipse depth δ_{true} to the observed depth δ_{obs} :

$$\delta_{\text{obs}} = \delta_{\text{true}} \frac{F_{\text{comp}}}{F_{\text{total}}}, \quad (1)$$

where the total system flux and the flux from only the companion (“comp”) binary are labeled appropriately. The requirement that the eclipse is produced by stars and that $\delta_{\text{true}} < 0.5$ translates to a bound on the faintest possible blended companion system:

$$\Delta m < -\frac{5}{2} \log_{10} \left(\frac{0.5}{\delta_{\text{obs}}} \right). \quad (2)$$

For TOI 837 ($T = 9.93$), this implies that any stellar companion invoked to explain the transit depth must be brighter than $T = 15.07$. In Figure 5, we set the spatial limit to $2''$ based on the precision at which we have localized the transits using seeing-limited ground-based photometry.

If the transit were box-shaped, this argument could be extended to even more restrictive depths (*e.g.*, Seager & Mallén-Ornelas 2003; Vanderburg et al. 2019; Rizzuto et al. 2020). Since the transits of TOI 837 are grazing, the second and third contact points do not occur, and the shape of the transit is not restrictive.

3.1.2. Speckle Imaging

The contrast limits obtained through the SOAR *I*-band speckle imaging (Section 2.3) are shown in Figure 5. While “Star A” was detected in the SOAR images, our ground-based photometry rules it out as a possible source of the eclipse signal (Section 2.4). To convert the remaining contrast constraints to limits on the masses of bound companions, we used the Baraffe et al. (2003) models for sub-stellar mass objects and the MIST models for stellar mass objects (Paxton et al. 2011, 2013, 2015; Dotter 2016; Choi et al. 2016). We assumed that the system age was 35 Myr, so that companions would be at a plausible state of contraction.

To convert from theoretical effective temperatures and bolometric luminosities to expected magnitudes in instrumental bandpasses, we made the simplifying assumption that all sources had blackbody spectra. Using the theoretical

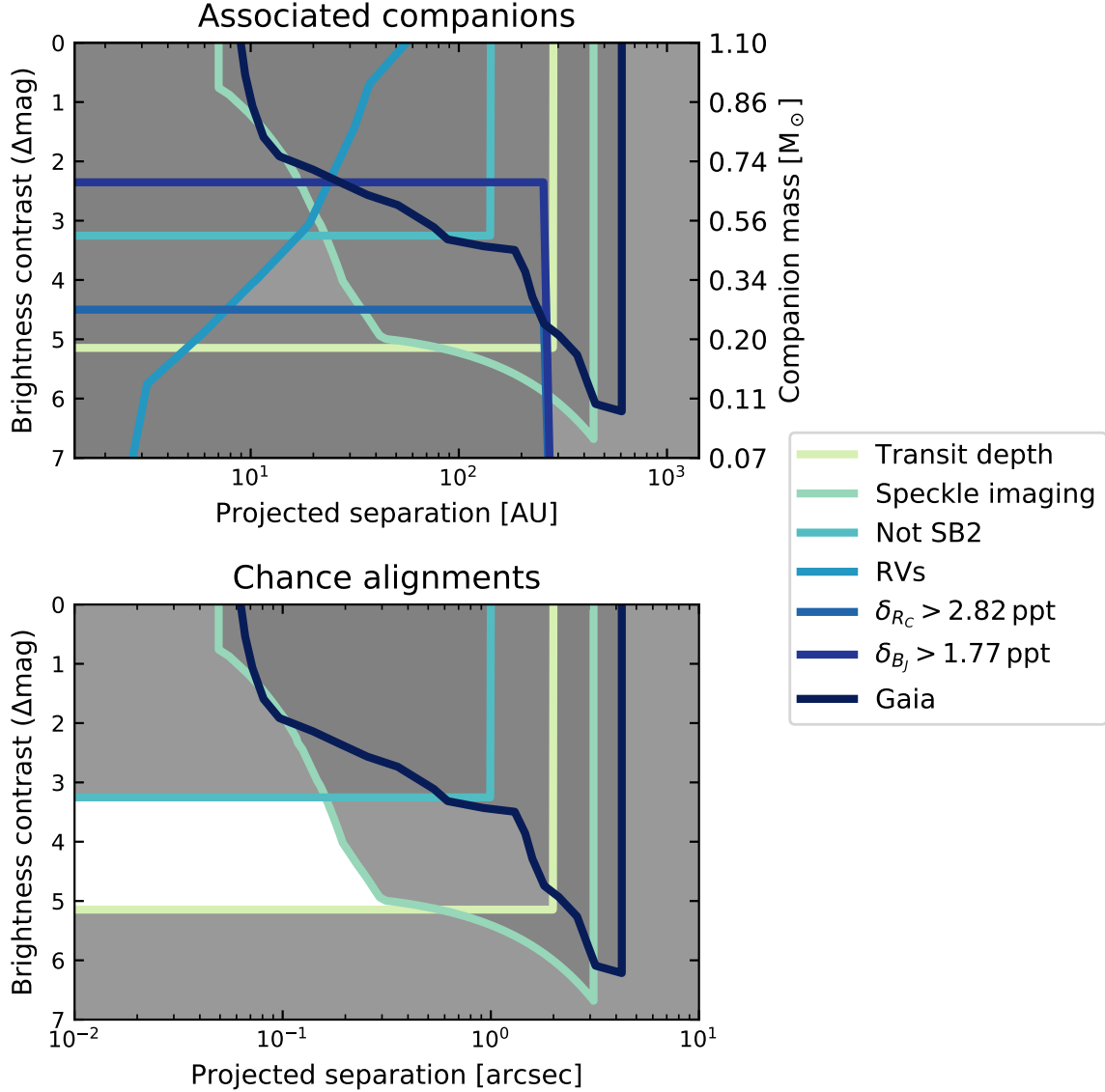


Figure 5. Astrophysical false positive scenarios. *Top:* for bound companions (EB and HEB scenarios), *Bottom:* for unassociated companions along the same line of sight (BEB scenarios). Each constraint is described in Section 3.1. Gray regions are ruled out by at least one constraint.

stellar parameters and the measured transmission functions (Tokovinin 2018), we then calculated the apparent magnitudes of stellar companions of different masses, and interpolated to produce the scale shown on the upper-right in Figure 5.

3.1.3. Not SB2

As described in Section 2.5.1, we searched the CCFs of the CHIRON spectra to determine whether TOI 837 is double-lined. For a stellar companion well-separated in velocity, this typically reveals companions with flux-fractions $F_2/F_1 \gtrsim 2\%$. For plotting purposes, in Figure 5 we have assumed a flux-fraction limit of 5% ($\Delta\text{mag} \approx 3.25$).

3.1.4. RVs

The combined radial velocities from FEROS, CHIRON, and Veloce can be used to detect massive bound companions

orbiting TOI 837. We searched for the presence of planetary and stellar-mass companions using *radvel* (Fulton et al. 2018). We assumed circular orbits, and performed two sets of fits.

For the first fit, we assumed a restrictive prior on the period and time of periaapse, using the known ephemeris from the transit. We then fitted for the semi-amplitude, instrument offsets, and jitter parameters. This yielded a non-detection of the planet’s orbit. The corresponding 3- σ (99.7th percentile) upper limit on $M_p \sin i$ is $1.20M_{\text{Jup}}$. The data and corresponding model are shown in Figure 4.

The above exercise ruled out the possibility that the observed eclipses are caused by a stellar-mass object orbiting TOI 837. The lack of a linear trend in the radial velocities, particularly in the FEROS data, further constrains the presence of a hierarchical binary system. To derive limits for

this second possibility, we placed a wide log-uniform prior on the semi-amplitude and period ($\log K [\text{ms}^{-1}] \sim \mathcal{U}(1, 10^5)$, $\log P [\text{days}] \sim \mathcal{U}(0.1, 10^{15})$). We then fitted for the semi-amplitude, period, time of conjunction, instrument offsets, and jitter parameters. We converted the resulting posterior in period and semi-amplitude to minimum mass and semi-major axis assuming Kepler’s third law. The resulting 3σ limits are shown in Figure 5.

3.1.5. Multicolor Photometry

Multicolor photometry and HEB scenarios—The most plausible HEB scenarios for TOI 837 involve pairs of eclipsing M dwarfs (Figure 5). Eclipses of such stars are much redder than eclipses of the G-dwarf TOI 837. Limits on whether the transit depth decreases in bluer bandpasses can therefore rule out some HEB scenarios.

We fitted for the observed depths in different bandpasses using a similar machinery as described in Section 4.3. We fitted each ground-based transit individually for the planet-to-star size ratio, the impact parameter, and a local quadratic trend (the ephemeris was assumed from an initial fit of only the TESS data). The corresponding $2\text{-}\sigma$ limits on the transit depths in Cousins-R and Johnson-B band light curves were 2.82 and 1.77 ppt, respectively, and are shown in Figure 2. Particularly in our Johnson-B light curve, the transit depth is correlated with the mean and linear slope of the light curve: a smaller depth is allowed if the data are fitted with a larger linear slope and a larger mean. Our quoted limits marginalize over these correlations, and the depth measurement itself is nearly Gaussian.

To determine what classes of HEB are eliminated by these limits, we performed the following calculation. We assumed that each system was composed of the primary (TOI 837), plus a tertiary companion eclipsing a secondary companion every 8.3 days. For secondary masses ranging from 0.07 to $1.10 M_\odot$, and mass ratios (M_3/M_2) from 0.1 to 1, we then calculated the observed maximal eclipse depth caused by Star 3 eclipsing Star 2 in each observed bandpass. As before, we interpolated between mass, effective temperature, and radius assuming the MIST isochrones for a 35 Myr old system, and also assumed that each source had a blackbody spectrum. We used the transmission functions from the SVO filter profile service³. For a typical HEB system (*e.g.*, $M_2 = M_3 = 0.2 M_\odot$), the bluest optical bandpasses produced eclipses roughly 10 times shallower than in TESS-band, because the M-dwarf blackbody function turns over at much redder wavelengths than the G-dwarf blackbody (Wien’s law).

For a fixed secondary mass, we then asked whether any tertiary companions existed for which the maximal expected eclipse depth could have been larger than the observed depth. In cases for which the answer was yes, we could not rule out such hierarchical eclipsing binary systems. Conversely, we were ruled out systems for which at fixed secondary mass no tertiary mass could enable eclipses of the necessary depth (in

R_C-band, or in B_J-band). The R_C-band limit corresponded to a secondary mass limit of $M_2 > 0.27 M_\odot$, and the B_J-band corresponded to a stronger limit of $M_2 > 0.70 M_\odot$.

Multicolor photometry and BEB scenarios—While the above constraints rule out HEBs, certain configurations of BEB systems (*e.g.*, a background G2V+K6V binary) can produce blue eclipses while remaining undetected along the line of sight. Such scenarios are constrained by the lack of an observed secondary eclipse, and therefore require either eccentric orbits to avoid secondary eclipses, or else a background twin binary system at double the orbital period. The only way to definitively rule out such scenarios is to prove that the loss of light is from the target star, for instance by detecting the Rossiter-McLaughlin effect during a transit.

3.1.6. Gaia

The “Gaia” curve in Figure 5 combines both point-source detections from imaging, and sources that show an astrometric excess. The curve was interpolated from Figure 4 of [Rizuto et al. \(2018\)](#). TOI 837 has a RUWE statistic of 1.022, indicative that there are no obviously present astrometric companions. The UWE statistic (square-root of the reduced astrometric χ^2) is 1.38, which is consistent with stars of similar brightness and color ([Lindgren et al. 2018](#), Appendix A).

3.1.7. Patient Imaging

Archival SERC-J and AAO-SES plates are available for the TOI 837 field⁴. These plates were acquired in 1982 and 1992, respectively. For high proper motion stars archival imagery can be used to detect slowly moving background stars that might be an astrophysical false-positive source (*e.g.*, [Huang et al. 2018](#), [Vanderburg et al. 2019](#)). However TOI 837 has only moved $\approx 0.7''$ between 1982 and present, in comparison to the $\approx 2.0''$ FWHM of the target on the plates. We therefore cannot resolve it with great confidence from background sources not already resolved through more modern imaging.

3.2. False positive probability

The constraints on false-positive scenarios summarized in Figure 5 rule out the possibilities that *i*) the eclipses are caused by a star orbiting TOI 837, *ii*) the eclipses are caused by hierarchical blends, and *iii*) the eclipses are caused by neighboring stars outside $\approx 2''$. The only scenario not formally ruled out is a background eclipsing binary. A simple (fallacious) argument on the a priori probability of background blends follows from counting statistics. The local density of $T < 15.1$ stars around TOI 837, found by counting from TIC8, is $3.7 \times 10^{-4} \text{ arcsec}^{-2}$. Therefore within the relevant $\approx 0.3''$ radius not excluded by the SOAR HRCam contrast curve, for a randomly selected star we would expect 1.0×10^{-4} potential $T < 15.1$ contaminants, which appears small.

³ <http://svo2.cab.inta-csic.es/theory/fps/>

⁴ https://archive.stsci.edu/cgi-bin/dss_form

The reason the above statement is an insufficient argument against BEBs is that TOI 837 is not a randomly selected star—it was selected because it shows eclipses. Given a foreground star that shows eclipses, the probability of a background star being present is much greater than for an arbitrary foreground star. The relevant populations need to be modelled at the Monte Carlo level. We opt to use VESPA to perform this population modelling (Morton 2012, 2015b).

VESPA calculates the false positive probability for a transit signal as

$$\text{FPP} = 1 - P_{\text{pl}}, \quad (3)$$

where in our case the probability that the signal comes from a planet, P_{pl} , is given by

$$P_{\text{pl}} = \frac{\mathcal{L}_{\text{pl}}\pi_{\text{pl}}}{\mathcal{L}_{\text{pl}}\pi_{\text{pl}} + \mathcal{L}_{\text{BEB}}\pi_{\text{BEB}}}, \quad (4)$$

where \mathcal{L}_i is the model likelihood for the planet and BEB scenarios, and π_i is the model prior. The terms labelled as “BEB” usually include other false positive scenarios (HEBs and EBs), but our followup data have excluded these possibilities. The priors are evaluated using a combination of galactic population synthesis (Girardi et al. 2005), binary star statistics (Raghavan et al. 2010), and specific planet occurrence rates (Morton 2012, Section 3.4). The likelihoods are evaluated by forward-modelling a representative population of eclipsing bodies for model class, in which each population member has a particular trapezoidal eclipse depth, total duration, and ingress duration. The likelihood is then calculated by multiplying the probability distribution function of simulated population’s shape parameters with the posterior probability of the actual observed eclipse shape.

We ran VESPA⁵, and directly incorporated our constraints of the SOAR *I*-band contrast curve and a non-detection of secondary eclipses with a depth set at roughly twice the limits from the SPOC vetting report (0.1%). We verified that changing the secondary eclipse depth limit did not significantly affect the results. We set the maximum aperture radius at 2'', based on our ground-based photometry. Incorporating the constraints from Figure 5, our nominal false positive probability analysis excluded EB and HEB scenarios. This yielded an FPP of 0.21% for TOI 837.01, sufficient for formal validation as a planet (Morton 2012). We did not incorporate our constraint that TOI 837 is not double-lined, which rules out an additional portion of BEB parameter space. Had we not acquired multicolor ground-based photometry, and been unable to exclude HEB scenarios, the FPP would have risen to 8%. Since the transits are achromatic (Figure 2), particularly in Johnson-B band, we can rule out HEB scenarios.

4. SYSTEM MODELLING

4.1. The Cluster

4.1.1. Physical Characteristics

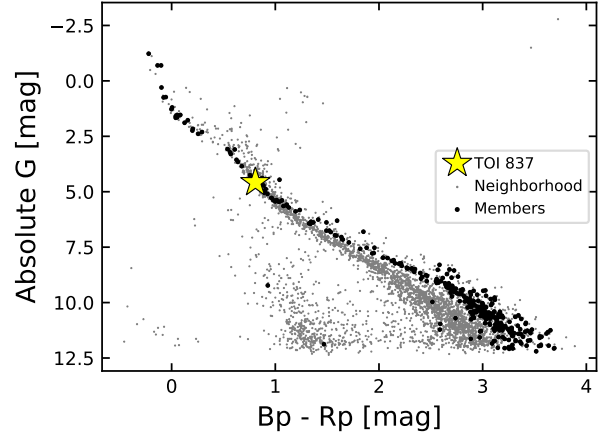


Figure 6. Hertzsprung-Russell diagram of TOI 837 and members of IC 2602. Members (black circles) were identified by Cantat-Gaudin et al. (2018). Gray circles are non-member stars within 5 standard deviations of the mean IC 2602 right ascension, declination, and parallax. G denotes Gaia broadband magnitudes, Bp Gaia blue, and Rp Gaia red.

Table 1. Previously reported ages for the open cluster IC 2602.

Method	Age [Myr]	Reference
MSTO isochrone	36.3	Mermilliod (1981)
PMS+MSTO isochrone	30 ± 5	Stauffer et al. (1997)
Isochrone (a)	67.6	Kharchenko et al. (2005)
Isochrone (b)	221	Kharchenko et al. (2013)
Isochrone	67.6	van Leeuwen (2009)
LDB (c)	46^{+6}_{-5}	Dobbie et al. (2010)
MSTO isochrone (d)	41–46	David & Hillenbrand (2015)
MSTO isochrone (e)	37–43	David & Hillenbrand (2015)
Li selection + isochrone	$43.7^{+4.3}_{-3.9}$	Bravi et al. (2018)
Isochrone (f)	30^{+9}_{-7}	Randich et al. (2018)
LDB	$43.7^{+4.3}_{-3.9}$	Randich et al. (2018)
Isochrone	$35.5^{+0.8}_{-1.6}$	Bossini et al. (2019)
Isochrone	$35.5^{+14.6}_{-10.4}$	Kounkel & Covey (2019)

NOTE— MSTO \equiv main sequence turn-off. PMS \equiv pre-main-sequence. LDB \equiv lithium depletion boundary. (a) Based on location in HR diagram of just two stars. (b) Notes major age change since Kharchenko et al. (2005). (c) Dobbie et al. (2010) performed a dedicated study of the LDB in IC 2602. Comparing to early isochronal ages, they write their age is “consistent with the general trend delineated by the Pleiades, α -Per, IC 2391, and NGC 2457, whereby the LDB age is 120–160 per cent of the estimates derived using more traditional techniques” such as isochrone fitting. (d) Using Ekström et al. (2012) evolutionary models. (e) Using PARSEC evolutionary models (Bressan et al. 2012). (f) Averaged across PROSECCO, PARSEC, MIST models in (J, H, K_s) and (J, H, K_s, V) planes.

The IC 2602 cluster is about 150pc from the Earth, and is near the galactic plane with $(l, b) \approx (289.6^\circ, -5.0^\circ)$ (Cantat-Gaudin et al. 2018). It is also sometimes called the θ Carinae cluster, after its brightest member. While IC 2602 is close to the Lower Centaurus Crux subgroup of the Scorpio-Centaurus OB2 association in both position and proper motion space, its older age and clear kinematic separation indicate that it is a distinct stellar population (de Zeeuw et al. 1999; Damiani et al. 2019).

⁵ We used VESPA-0.6 and isochrones-1.2.2.



Figure 7. Positions and kinematics of TOI 837 (star), IC 2602 members (black circles), and stars in the neighborhood (gray circles). Members were identified by [Cantat-Gaudin et al. \(2018\)](#). α denotes right ascension, δ declination, π parallax, μ_δ and μ_α proper motion in each equatorial direction, and RV radial velocity reported by Gaia DR2. The RVs are for unblended spectra of bright stars ($G \lesssim 12$). The proper motion projection (μ_δ vs. $\mu_\alpha \cos \delta$) highlights incompleteness in the membership selection function.

Reliable ages reported for IC 2602 range from 30–46 Myr. We have collected ages reported over the years in Table 1. The Li depletion boundary technique yields slightly older absolute ages than isochrone fitting ([Dobbie et al. 2010](#); [Randich et al. 2018](#)). Rather than redetermine the age of the cluster and add another line to the table, we simply adopt an absolute age range for TOI 837 of 30–46 Myr.

Reported mean metallicity values $[\text{Fe}/\text{H}]$ for the cluster range between slightly super-solar (0.04 ± 0.01 , [Baratella et al. 2020](#)) and slightly sub-solar (-0.02 ± 0.02 , [Netopil et al. 2016](#)). The extinction $E(B-V)$ is rather low, with reported values ranging from 0.03 to 0.07 (*e.g.*, [Randich et al. 2018](#)).

Kinematically, IC 2602 seems to be supervirial, in the sense that the observed stellar velocity dispersion is larger than the value expected if it were in virial equilibrium by about a factor of two ([Bravi et al. 2018](#)). [Damiani et al. \(2019\)](#) also reported evidence for the ongoing evaporation of IC 2602, in the form of a diffuse $\approx 10^\circ$ halo of young stars around the central density cusps. A gyrochronological study of these stars could confirm that these stars are truly coeval with the cluster.

4.1.2. HR Diagram

Figure 6 shows a Hertzsprung-Russell diagram of TOI 837, the IC 2602 cluster, and the “neighborhood” of spatially nearby stars. Stars labelled as “cluster members” are those reported by [Cantat-Gaudin et al. \(2018\)](#) based on Gaia DR2 positions, proper motions, and parallaxes. We included candidate members with formal membership probability exceeding 10%. Save for a few low-mass outliers, most members appear to be young and coeval.

TOI 837 is in its expected position relative to the other members along the cluster isochrone. This photometrically limits the presence of binary companions in the TOI 837 system, to within perhaps half the brightness (≈ 0.75 magnitudes) of the target star.

Figure 6 also suggests that the membership census of IC 2602 is incomplete. We defined the reference “neighborhood” as the group of at most 10^4 randomly selected non-member stars within 5 standard deviations of the mean IC 2602 right ascension, declination, and parallax. We queried Gaia DR2 for these stars using *astroquery* ([Ginsburg et al. 2018](#)). Many low-mass stars appear above the

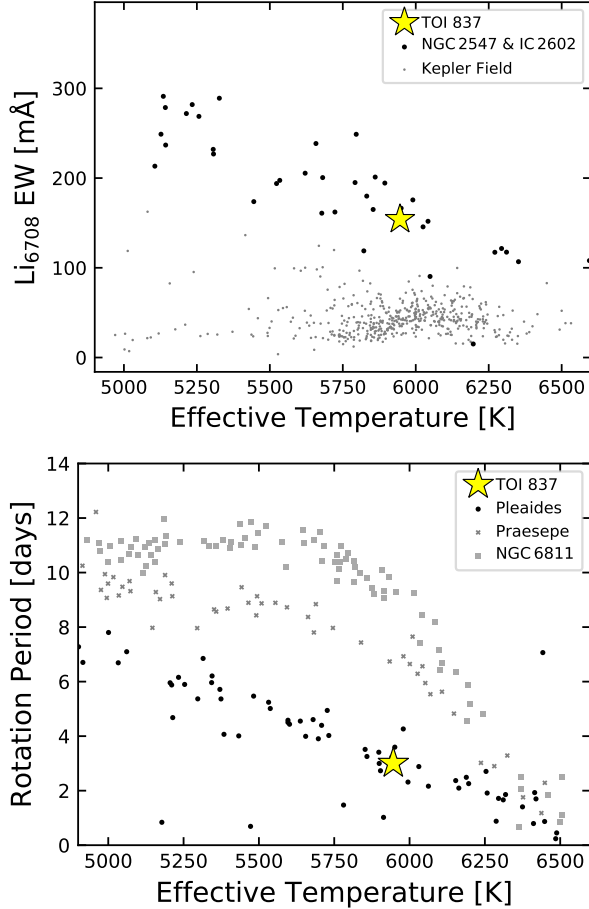


Figure 8. Youth diagnostics. *Top:* Lithium 6708Å equivalent widths for TOI 837, field stars, and young open clusters. The field star sample is drawn from Kepler planet hosts, and was measured by [Berger et al. \(2018\)](#) using Keck-HIRES. The young open clusters members were surveyed by [Randich et al. \(2018\)](#) using the UVES and GIRAFFE spectrographs at the ESO VLT. [Randich et al. \(2018\)](#) found lithium depletion boundary ages for these clusters of $37.7^{+5.7}_{-4.8}$ Myr (NGC2547) and $43.7^{+4.3}_{-3.9}$ Myr (IC 2602). *Bottom:* Rotation periods for TOI 837 and selected open clusters. The Pleiades (120Myr), Praesepe (670Myr), and NGC6811 (1000Myr) are shown. Their rotation periods were measured by [Rebull et al. \(2016\)](#); [Douglas et al. \(2017, 2019\)](#), and [Curtis et al. \(2019a\)](#), respectively.

main sequence, even though they were not identified as 5-dimensional kinematic members through the unsupervised [Cantat-Gaudin et al. \(2018\)](#) membership assignment process.

4.2. The Star

4.2.1. Membership of TOI 837 in IC 2602

TOI 837 has been reported as a member of IC 2602 by many independent investigators (*e.g.*, [Kharchenko et al. 2013](#); [Oh et al. 2017](#); [Cantat-Gaudin et al. 2018](#); [Damiani et al. 2019](#); [Kounkel & Covey 2019](#)). The simplest way to

verify the membership is through inspection of the Gaia DR2 position and kinematics. Figure 7 shows the six-dimensional positions and kinematics of TOI 837, IC 2602 members, and nearby stars. The “neighborhood” is defined as in Figure 6. The axes limits for the right ascension, declination, and parallax dimensions are set by being within 5 standard deviations of the mean IC 2602 right ascension, declination, and parallax. The axes limits for the proper motion and radial velocity dimensions are set at the 25th and 75th percentiles, in order to give a sense of the population’s distribution, while excluding outliers. The radial velocities suffer the greatest incompleteness due to the current $G \approx 12$ magnitude limit of the Gaia DR2 data processing.

Figure 7 provides strong evidence that TOI 837 is a member of IC 2602. The only dimension that could lead to some worry is the parallax, as TOI 837 is one of the closest IC 2602 members reported by [Cantat-Gaudin et al. \(2018\)](#). Fortunately, there are independent means of verifying the star’s youth.

4.2.2. Rotation

As stars get older, their rotation rates incrementally slow due to magnetic braking [Weber & Davis \(1967\)](#); [Skumanich \(1972\)](#). One way to verify the youth of TOI 837 is by comparing its rotation period to other stars with known ages.

We measured the rotation period from the PDCSAP light curve using the Lomb-Scargle periodogram implemented in *astropy* ([Lomb 1976](#); [Scargle 1982](#); [VanderPlas & Ivezic 2015](#)). We fitted the light curve without masking out the transits or flares, as these represent a small fraction of the overall time series. To derive the uncertainty on the best period, we fitted a gaussian to the dominant peak, after first ensuring that we had oversampled the initial frequency grid. This gave a rotation period of $P_{\text{rot}} = 2.987 \pm 0.056$ d when allowing for a single Fourier terms in the periodogram model, and $P_{\text{rot}} = 3.004 \pm 0.053$ d when allowing for two Fourier terms. As the second model provides a better fit to the data, we adopt the second measurement.

As we will discuss in Section 4.2.4, we measured the star’s radius by combining the spectroscopic effective temperature with a broadband photometry SED fit. We would expect, combining our R_* and P_{rot} measurements, that the equatorial velocity v of the star would be 17.67 ± 0.32 km s⁻¹. Our spectroscopically measured $v \sin i$ from CHIRON, 17.48 ± 0.15 km s⁻¹ agrees reasonably well with this expectation.

The star is clearly a rapid rotator. Figure 8 compares its rotation period with rotation periods that have been measured in a number of well-studied open clusters. TOI 837 seems to be gyrochronologically coeval with the Pleiades sequence. This is not to say that TOI 837 is “Pleiades-aged”, because the observed scatter in the rotation-period diagram for the first 10–100 Myr is quite high (see Figure 9 of [Rebull et al. 2020](#)). Instead, we interpret the rotation period as evidence to support the claim that TOI 837 is younger than ~ 500 Myr.

4.2.3. Lithium

Lithium depletion for early G-dwarfs like TOI 837 requires hundreds of megayears (Soderblom et al. 2014). This is because their convective envelopes are shallow, and so transport of photospheric lithium to the hot core takes place over diffusive timescales, rather than convective timescales. Nonetheless, comparison of early G-dwarfs in the field to *e.g.*, 600 Myr old Hyads has shown that the depletion does indeed happen over many gigayears (Berger et al. 2018).

The spectra of TOI 837 all show the 6708 Å lithium doublet in absorption. Opting to use our FEROS spectra because of their high S/N, we measured the line’s equivalent width (EW) to be 154 ± 9 mÅ. Figure 8 compares this EW to stars in the field, and other young open cluster members. The field star measurements were collected by Berger et al. (2018); we show their reported lithium detections with $S/N > 3$. The young open cluster members were selected for the presence of lithium, as described by Randich et al. (2018). The measured TOI 837 Li EW is much larger than observed for field stars, and is consistent with lithium absorption seen in stars with similar colors in sub-100 Myr moving groups.

4.2.4. Stellar Parameters

Select properties of TOI 837 from the literature and our analysis are presented in Table 2. The spectroscopic parameters were measured from each of the six CHIRON spectra (Section 2.5.1). We then averaged the results, and adopted the standard deviation across the spectra as the uncertainty.

We then calculated the stellar radius and reddening following Stassun et al. (2017). We first derived the bolometric flux by combining available broadband magnitudes from Gaia, Tycho-2, APASS, 2MASS, and WISE. We then fitted the SED with the Kurucz (2013) stellar atmosphere models, and summed to find F_{bol} . When fitting the atmosphere model, we varied the extinction (A_V) and the overall normalization. This procedure yielded $A_V = 0.20 \pm 0.03$, which independently agrees with the average from the IC 2602 isochrone fits of Randich et al. (2018). We then combined the spectroscopic effective temperature, bolometric flux, and Gaia distance to determine the stellar radius, using the Stefan-Boltzmann law.

4.3. The Planet

We fitted the available time-series photometry of TOI 837.01 as follows. For the PDCSAP light curve, we first eliminated points that had quality flags corresponding to any of bits {3, 4, 6, 8, 11, 12}. This excluded cadences affected by coarse spacecraft pointing, reaction wheel desaturation events, manual flags, cosmic ray hits, and straylight from the Earth or Moon being present. Inspecting the data, we also manually excluded the two flares shown in Figure 1. We then trimmed the TESS data to windows of ± 7 hr centered on each transit.

Our joint model for the TESS and ground-based data was a Agol et al. (2019) transit with physical and orbital parameters shared across all transit windows, plus a local quadratic trend allowed within each window. The parameters and priors are listed in Table 3. In brief, we fitted for the shared stellar parameters ($\log g, R_*, u_0, u_1$), and the shared planetary

Table 2. Literature and Measured Properties for TOI 837

Other identifiers			
TIC 460205581			
GAIA DR2 5251470948229949568			
Parameter	Description	Value	Source
$\alpha_{J2015.5}$	Right Ascension (RA)	10:28:08.95	1
$\delta_{J2015.5}$	Declination (Dec)	-64:30:18.76	1
B	Johnson B mag.	11.119 ± 0.107	2
V	Johnson V mag.	10.635 ± 0.020	2
G	Gaia G mag.	10.356 ± 0.020	1
Bp	Gaia Bp mag.	10.695 ± 0.020	1
Rp	Gaia Rp mag.	9.887 ± 0.020	1
T	TESS mag.	9.9322 ± 0.006	2
J	2MASS J mag.	9.392 ± 0.030	3
H	2MASS H mag.	9.108 ± 0.038	3
K _S	2MASS K _S mag.	8.933 ± 0.026	3
W1	WISE1 mag.	8.901 ± 0.023	4
W2	WISE2 mag.	8.875 ± 0.021	4
W3	WISE3 mag.	8.875 ± 0.020	4
W4	WISE4 mag.	$8.936 \pm \text{N/A}$	4
π	Gaia DR2 parallax (mas)	6.989 ± 0.022	1
d	Distance (pc)	143.1 ± 0.5	1
μ_α	Gaia DR2 proper motion in RA (mas yr ⁻¹)	-18.017 ± 0.039	1
μ_δ	Gaia DR2 proper motion in DEC (mas yr ⁻¹)	11.307 ± 0.037	1
RV	Systemic radial velocity (km s ⁻¹)	$17.44 \pm 0.64^\dagger$	1
$v \sin i_*$	Rotational velocity (km s ⁻¹)	17.48 ± 0.15	5
[Fe/H]	Metallicity	-0.065 ± 0.035	5
T_{eff}	Effective Temperature (K)	5946 ± 39	5
$\log g_*$	Surface Gravity (cgs)	4.48 ± 0.03	5
Li EW	6708 Å Equiv. Width (mÅ)	154 ± 9	6
P_{rot}	Rotation period (d)	3.004 ± 0.053	7
Age	Adopted stellar age (Myr)	30–46	8
Spec. Type	Spectral Type	G0V	8
R_*	Stellar radius (R_\odot)	1.049 ± 0.019	9
F_{bol}	Stellar bolometric flux (cgs)	$(1.967 \pm 0.046) \times 10^{-9}$	9
A_V	Interstellar reddening (mag)	0.20 ± 0.03	9

NOTE—[†] Systemic RV uncertainty is the standard deviation of single-transit radial velocities, as quoted in Gaia DR2. Provenances are: ¹Gaia Collaboration et al. (2018), ²Stassun et al. (2019), ³Skrutskie et al. (2006), ⁴Wright et al. (2010), ⁵CHIRON spectra, ⁶FEROS spectra, ⁷TESS light curve, ⁸IC 2602 ages from isochrone & lithium depletion analyses (see Section 4.1.1), ⁹Combined photometric SED fit and spectroscopic parameters.

parameters ($t_0, P, b, \log(R_p/R_*)$). There were also three free trend parameters for each of the nine transits to account for the rotational variability. This yielded a total of 35 free parameters, of which 8 have physical relevance, and 27 are nuisance parameters.

We fitted the model using PyMC3 (Salvatier et al. 2016; Theano Development Team 2016). For the exoplanet transit, we used the exoplanet code (Foreman-Mackey et al. 2020). After initializing each model with the parameters of the maximum *a posteriori* model, we assumed a Gaussian likelihood, and sampled using PyMC3’s gradient-based No-

Table 3. Best-fit transit model priors and posteriors.

Param.	Unit	Prior	Median	Mean	Std. Dev.	3%	97%
P	d	$\mathcal{N}(8.3247; 0.0050)$	8.3249313	8.3249314	0.0000218	8.3248923	8.3249736
$t_0^{(1)}$	d	$\mathcal{N}(1574.273800; 0.0050)$	1574.2723593	1574.2723618	0.0005840	1574.2712581	1574.2734293
$\log R_p/R_*$	—	$\log \mathcal{U}(0.01; 1.00)$	-2.27145	-1.93679	0.75322	-2.59835	-0.20204
b	—	$\mathcal{U}(0; 1 + R_p/R_*)$	0.9867	1.0991	0.2506	0.9259	1.7389
u_1	—	$\mathcal{U}(0.186; 0.486)^{(2)}$	0.378	0.366	0.083	0.220	0.486
u_2	—	$\mathcal{U}(0.075; 0.375)^{(2)}$	0.266	0.253	0.083	0.107	0.375
R_*	R_\odot	$\mathcal{T}(1.05; 0.06)$	1.07	1.07	0.06	0.96	1.17
$\log g$	cgs	$\mathcal{N}(4.48; 0.09)$	4.38	4.38	0.07	4.26	4.52
$a_{0,\text{TESS}}$	—	$\mathcal{N}(1.00; 0.01)$	0.9985	0.9985	0.0001	0.9983	0.9987
$a_{1,\text{TESS}}$	d^{-1}	$\mathcal{U}(-0.10; 0.10)$	-0.0004	-0.0004	0.0003	-0.0010	0.0002
$a_{2,\text{TESS}}$	d^{-2}	$\mathcal{U}(-0.10; 0.10)$	-0.0176	-0.0176	0.0023	-0.0217	-0.0132
$a_{0,\text{TESS}}$	—	$\mathcal{N}(1.00; 0.01)$	1.009	1.009	0.0001	1.0088	1.0091
$a_{1,\text{TESS}}$	d^{-1}	$\mathcal{U}(-0.10; 0.10)$	-0.0138	-0.0138	0.0003	-0.0144	-0.0132
$a_{2,\text{TESS}}$	d^{-2}	$\mathcal{U}(-0.10; 0.10)$	-0.0543	-0.0544	0.0022	-0.0585	-0.0504
$a_{0,\text{TESS}}$	—	$\mathcal{N}(1.00; 0.01)$	0.9991	0.9991	0.0001	0.9990	0.9993
$a_{1,\text{TESS}}$	d^{-1}	$\mathcal{U}(-0.10; 0.10)$	0.0156	0.0156	0.0004	0.0150	0.0163
$a_{2,\text{TESS}}$	d^{-2}	$\mathcal{U}(-0.10; 0.10)$	0.0239	0.0238	0.0023	0.0193	0.0281
$a_{0,\text{TESS}}$	—	$\mathcal{N}(1.00; 0.01)$	1.0013	1.0013	0.0001	1.0011	1.0014
$a_{1,\text{TESS}}$	d^{-1}	$\mathcal{U}(-0.10; 0.10)$	0.0021	0.0021	0.0004	0.0014	0.0029
$a_{2,\text{TESS}}$	d^{-2}	$\mathcal{U}(-0.10; 0.10)$	-0.009	-0.0089	0.0028	-0.0141	-0.0035
$a_{0,\text{TESS}}$	—	$\mathcal{N}(1.00; 0.01)$	0.9906	0.9906	0.0001	0.9904	0.9908
$a_{1,\text{TESS}}$	d^{-1}	$\mathcal{U}(-0.10; 0.10)$	0.0015	0.0015	0.0003	0.0009	0.0021
$a_{2,\text{TESS}}$	d^{-2}	$\mathcal{U}(-0.10; 0.10)$	0.0318	0.0318	0.0023	0.0274	0.0362
$a_{0,\text{Sauce}}$	—	$\mathcal{N}(1.00; 0.01)$	0.9994	0.9994	0.0001	0.9992	0.9997
$a_{1,\text{Sauce}}$	d^{-1}	$\mathcal{U}(-0.10; 0.10)$	-0.0025	-0.0025	0.0023	-0.0069	0.0017
$a_{2,\text{Sauce}}$	d^{-2}	$\mathcal{U}(-0.10; 0.10)$	0.0693	0.0624	0.0297	0.0083	0.1
$a_{0,\text{Sauce}}$	—	$\mathcal{N}(1.00; 0.01)$	0.9996	0.9996	0.0001	0.9994	0.9999
$a_{1,\text{Sauce}}$	d^{-1}	$\mathcal{U}(-0.10; 0.10)$	0.0012	0.0012	0.0021	-0.0030	0.0050
$a_{2,\text{Sauce}}$	d^{-2}	$\mathcal{U}(-0.10; 0.10)$	0.0748	0.0694	0.0243	0.0263	0.1
$a_{0,\text{Sauce}}$	—	$\mathcal{N}(1.00; 0.01)$	0.9998	0.9998	0.0002	0.9995	1.0002
$a_{1,\text{Sauce}}$	d^{-1}	$\mathcal{U}(-0.10; 0.10)$	0.0016	0.0016	0.0031	-0.0043	0.0074
$a_{2,\text{Sauce}}$	d^{-2}	$\mathcal{U}(-0.10; 0.10)$	-0.0102	-0.0079	0.0505	-0.0991	0.0763
$a_{0,\text{Sauce}}$	—	$\mathcal{N}(1.00; 0.01)$	0.9995	0.9995	0.0003	0.9990	1.
$a_{1,\text{Sauce}}$	d^{-1}	$\mathcal{U}(-0.10; 0.10)$	0.0096	0.0095	0.0069	-0.0038	0.0222
$a_{2,\text{Sauce}}$	d^{-2}	$\mathcal{U}(-0.10; 0.10)$	0.0135	0.0097	0.0569	-0.0840	0.1
R_p/R_*	—	—	0.10	0.21	0.23	0.07	0.80
ρ_*	g cm^{-3}	—	1.17	1.19	0.20	0.85	1.56
R_p	R_{Jup}	—	1.08	2.18	2.43	0.68	8.24
a/R_*	—	—	16.22	16.27	0.89	14.69	17.94
$\cos i$	—	—	0.06	0.07	0.02	0.05	0.11
T_{14}	hr	—	1.94	1.94	0.05	1.85	2.03
T_{13}	hr	—	0.20	0.21	0.10	0.02	NaN

NOTE— T_{13} is ill-defined for a grazing transit. \mathcal{U} denotes a uniform distribution, \mathcal{N} a normal distribution, and \mathcal{T} a truncated normal bounded between zero and an upper limit much larger than the mean. (1) To convert mean TESS mid-transit time from BTJD to BJD_{TDB}, add 2,457,000. (2) Assuming an informative quadratic limb-darkening prior with uniform values about those given for the appropriate T_{eff} and $\log g$ from [Claret \(2017\)](#).

U-Turn Sampler ([Hoffman & Gelman 2014](#)). We used \hat{R} as our convergence diagnostic ([Gelman & Rubin 1992](#)).

While alternative approaches are available for simultaneously fitting space and ground based photometry (in addition to radial velocimetry), we opted for this approach because *i*) the radial velocimetry on its own did not show evidence for a planetary signal, and *ii*) we expected that this approach would provide the best measurement of the planetary ephemeris, which is key for follow-up efforts. The assumption of a constant radius across all bandpasses was tested by independently fitting each ground-based transit while letting

the planetary radius float (Section 3.1.5). The transit depths did not significantly change between different bandpasses.

The posteriors from this procedure are given in Table 3. Crucially important is the point that the transit is grazing. The grazing geometry hinders our ability to infer the stellar density and planet-to-star size ratio. The relevant posterior probabilities are shown in Figure 9.

The available data for TOI 837 put us in an odd position. The transit data provide a minimum size due to the grazing geometry; the radial velocity data provide a maximum mass ($\approx 1.20 M_{\text{Jup}}$). We could combine the two with an

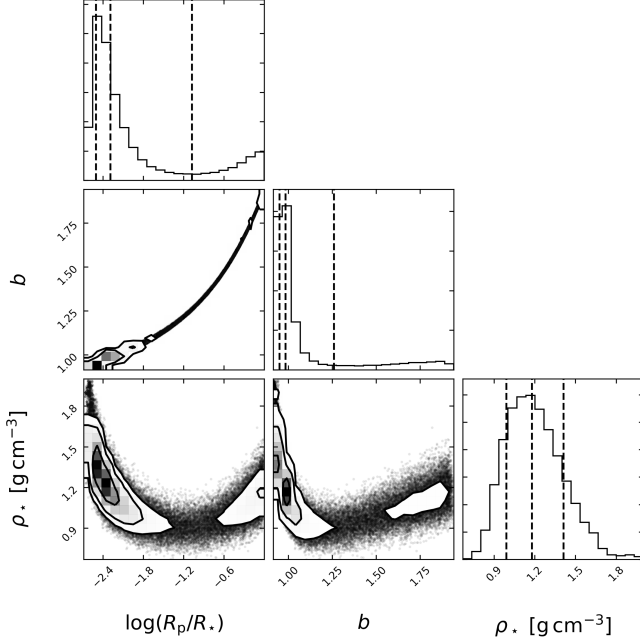


Figure 9. Posterior probabilities of impact parameter, planet-to-star size ratio, and stellar density. The photometric data fitted in Section 4.3 allow for nonphysical planet sizes ($R_p > 2R_{\text{Jup}}$; $\log(R_p/R_*) \gtrsim -1.6$) due to a classic degeneracy between the planet size and impact parameter. Non-planetary sizes would imply non-planetary masses, which are ruled out by our radial velocity measurements. This plot was made using `corner` (Foreman-Mackey 2016).

empirically-calibrated planetary mass-radius relation to force a more restrictive upper bound on the planetary size (e.g., Chen & Kipping 2016). The result of such an exercise would tautologically be that the planet would be smaller than the largest known Jovian planets ($\approx 2R_{\text{Jup}}$). This would also imply that the impact parameter is slightly below unity. The planet’s size, in our eyes, would remain poorly constrained even if we were to do this exercise, so we opt to fit the photometry and radial velocities separately, to ensure clarity about which datasets are providing which constraints.

5. DISCUSSION

TOI 837 joins a number of other young planetary systems reported from TESS, including DS Tuc Ab, HIP 67522b, TOI 1726, and AU Mic b (Newton et al. 2019; Zhou et al. 2019; Montet et al. 2019; Rizzuto et al. 2020; Mann et al. 2020; Plavchan et al. 2020; Palle et al. 2020; Addison et al. 2020; Martioli et al. 2020; Hirano et al. 2020). Unlike these planets, TOI 837.01 is validated but not yet confirmed.

The easiest path towards definitively confirming whether TOI 837 is a planet will be a Rossiter-McLaughlin (RM) measurement. Detection of the RM signal would rule out BEB and HEB scenarios, as it would imply that the eclipsing object is bound to the target star. Combined with our non-detection of the planet’s mass from radial velocity monitoring, this would confirm that TOI 837.01 is a planet.

The maximum amplitude of the Rossiter-McLaughlin anomaly is (Gaudi & Winn 2007)

$$\Delta V_{\text{RM}} \approx f_{\text{LD}} \cdot \delta \cdot v \sin i \cdot \sqrt{1-b^2} \approx 14 \text{ m s}^{-1}, \quad (5)$$

for

$$f_{\text{LD}} = 1 - c_1(1-\mu) - c_2(1-\mu)^2, \quad (6)$$

where $\mu \approx (1-b^2)^{1/2}$, and for calculation purposes we assumed $b = 0.95$ and used stellar and transit parameters from Tables 2 and 3. Although challenging, for a 1.9 hr transit of a $V = 10.6$ star, a detection could be achieved with modern spectrographs. The next viable total transit windows from Chile occur in January and February of 2021; there are also a few visible per season from other southern locations.

The Rossiter-McLaughlin approach is more likely to yield short-term success than a direct mass measurement because of the RV noise expected to be induced by stellar rotation. The photometric amplitude induced by starspots on TOI 837 is $\approx 2\%$. The RV noise expected over the course of the ≈ 3 d rotation period can then be estimated by multiplying the photometric amplitude and spectroscopic equatorial velocity. This gives $\sigma_{\text{RV,rot}} \approx 300 \text{ m s}^{-1}$, and is consistent with the scatter we observe in our radial velocities from FEROS. Detecting a planet’s Doppler signal in these regimes is challenging, and requires a significant amount of data and care in signal extraction (Barragán et al. 2019). The Rossiter-McLaughlin measurement avoids the majority of this issue because the transit occurs over a much shorter duration than a single stellar rotation period.

If the RM measurements prove that the planet is real, a campaign to measure the mass timed to coincide with TESS sectors 36 and 37 (i.e., from late March to late May of 2021) would significantly ease the extraction of the planetary Doppler signal. The reason is that the radial velocities, activity indicators, and photometry could then be modeled simultaneously, which would greatly constrain any Gaussian process model for the spot-induced RV signal.

Table 4. TOI 837 photometry.

Time [BJD _{TDB}]	Rel. Flux	Rel. Flux Err.	Instrument
2451234.12345	1.00	0.01	TESS

NOTE— Table 4 is published in its entirety in a machine-readable format. An example entry is shown for guidance regarding form and content.

Table 5. TOI 837 radial velocities.

Time [BJD _{TDB}]	RV [m s^{-1}]	σ_{RV} [m s^{-1}]	Instrument
8669.533150	-57.80	27.50	FEROS
8669.540450	-13.90	29.40	FEROS
8676.506930	6.70	37.80	FEROS
8677.519150	-70.30	44.60	FEROS
8884.787630	240.00	28.00	CHIRON
8891.891180	-76.00	37.00	CHIRON

Table 5 continued

Table 5 (continued)

Time [BJD _{TDB}]	RV [m s ⁻¹]	σ_{RV} [m s ⁻¹]	Instrument
8898.735330	-10.00	43.00	CHIRON
8903.725760	-25.00	38.00	CHIRON
8904.739930	80.10	24.50	FEROS
8905.793630	88.00	21.70	FEROS
8908.762520	45.30	28.30	FEROS
8909.702140	0.00	31.80	FEROS
8912.606750	41.30	24.10	FEROS
8913.740580	161.10	37.30	FEROS
8915.762170	10.00	33.00	CHIRON
8916.714540	-93.50	33.60	FEROS
8917.765720	-159.70	24.80	FEROS
8920.706100	99.00	32.00	CHIRON
8922.845800	-148.30	54.90	FEROS
8915.924027	37.51	725.91	Veloce
8921.284950	105.90	453.19	Veloce
8922.733572	-195.92	195.63	Veloce
8924.583708	-7.65	262.32	Veloce
8926.365810	14.28	442.64	Veloce
8927.318146	207.04	505.19	Veloce
8928.559780	-7.28	180.24	Veloce
8930.324059	-2.60	152.02	Veloce
8931.293091	-45.68	152.94	Veloce
8932.065206	-105.60	319.82	Veloce

ACKNOWLEDGMENTS

TOI 837 was included on the TESS “short-cadence” target list in part thanks to the Guest Investigator program of G. Sacco (G011265). This paper includes data collected by the TESS mission, which are publicly available from the [Mikulski Archive for Space Telescopes \(MAST\)](https://heasarc.gsfc.nasa.gov/TESS/). Funding for the TESS mission is provided by NASA’s Science Mission directorate. The Digitized Sky Survey was produced by [Agol, E., Luger, R., & Foreman-Mackey, D. 2019, arXiv e-prints, 1908.03222](https://www.digitizedsky.org/). Figure 3 is based on photographic data obtained using the Oschin Schmidt Telescope on Palomar Mountain. This research made use of the Exoplanet Follow-up Observation Program website, which is operated by the California Institute of Technology, under contract with the National Aeronautics and Space Administration under 50-006-0696 planet Exploration Program. This research has made use of the SVO Filter Profile Service (http://svo2.cab.inta-csic.es/theory/fps/) supported from the Spanish MINECO through grant AYA2017-84089.

Baraffe, I., Chabrier, G., Barman, T. S., Allard, F., & Hauschildt,

P. H. 2003, *A&A*, 402, 701

Baratella, M., D’Orazi, V., Carraro, G., et al. 2020, *Astronomy and Astrophysics*, 634, A34

Barnes, S. A., Weingrill, J., Granzer, T., Spada, F., & Strassmeier, K. G. 2015, *Astronomy & Astrophysics*, 583, A73, arXiv: 1511.00554

Barragán, O., Aigrain, S., Kubyskhina, D., et al. 2019, *Monthly Notices of the Royal Astronomical Society*

Software: *astrobases* (Bhatti et al. 2018), *AstroImageJ* (Collins et al. 2017), *astropy* (Astropy Collaboration et al. 2018), *astroquery* (Ginsburg et al. 2018), *cdips-pipeline* (Bhatti et al. 2019), *corner* (Foreman-Mackey 2016), *exoplanet* (Agol et al. 2019), *exoplanet* (Foreman-Mackey et al. 2020), and its dependencies (Agol et al. 2019; Kipping 2013; Luger et al. 2019; Theano Development Team 2016). *IPython* (Pérez & Granger 2007), *isochrones* (Morton 2015a), *lightkurve* (Lightkurve Collaboration et al. 2018), *matplotlib* (Hunter 2007), *MESA* (Paxton et al. 2011, 2013, 2015), *numpy* (Walt et al. 2011), *pandas* (McKinney 2010), *pyGAM* (Servén et al. 2018), *PyMC3* (Salvatier et al. 2016), *radvel* (Fulton et al. 2018), *scipy* (Jones et al. 2001), *tesscut* (Brasseur et al. 2019), *VESPA* (Morton 2012, 2015b), *webplotdigitizer* (Rohatgi 2019), *wotan* (Hippke et al. 2019).

Facilities: *Astrometry:* Gaia (Gaia Collaboration et al. 2016, 2018). *Imaging:* Second Generation Digitized Sky Survey, SOAR (HRCam; Tokovinin 2018). *Spectroscopy:* CTIO1.5m (CHIRON; Tokovinin et al. 2013), MPG2.2m (FEROS; Kaufer et al. 1999), AAT (Veloce; Gilbert et al. 2018). *Photometry:* El Sauce:0.356m, TESS (Ricker et al. 2015).

REFERENCES

- Berger, T. A., Howard, A. W., & Boesgaard, A. M. 2018, *The Astrophysical Journal*, 855, 115
- Bhatti, W., Bouma, L., & Yee, S. 2019, *cdips-pipeline* v0.1.0, <https://doi.org/10.5281/zenodo.3370324>
- Bhatti, W., Bouma, L. G., & Wallace, J. 2018, *astrobases*, <https://doi.org/10.5281/zenodo.1469822>
- Biddle, L. I., Johns-Krull, C. M., Llama, J., Prato, L., & Skiff, B. A. 2018, *The Astrophysical Journal Letters*, 853, L34
- Borucki, W. J., Koch, D., Basri, G., et al. 2010, *Science*, 327, 977
- Bossini, D., Vallenari, A., Bragaglia, A., et al. 2019, *Astronomy and Astrophysics*, 623, A108
- Bouma, L. G., Hartman, J. D., Bhatti, W., Winn, J. N., & Bakos, G. Á. 2019, *ApJS*, 245, 13
- Brasseur, C. E., Phillip, C., Fleming, S. W., Mullally, S. E., & White, R. L. 2019, *Astrophysics Source Code Library*, ascl:1905.007
- Bravi, L., Zari, E., Sacco, G. G., et al. 2018, *Astronomy and Astrophysics*, 615, A37
- Bressan, A., Marigo, P., Girardi, L., et al. 2012, *Monthly Notices of the Royal Astronomical Society*, 427, 127

- Brucalassi, A., Koppenhoefer, J., Saglia, R., et al. 2017, *Astronomy and Astrophysics*, 603, A85
- Burke, C. J., Gaudi, B. S., DePoy, D. L., & Pogge, R. W. 2006, *The Astronomical Journal*, 132, 210
- Cameron, A. G. W., & Ward, W. R. 1976, 7, conference Name: Lunar and Planetary Science Conference
- Cantat-Gaudin, T., Jordi, C., Vallenari, A., et al. 2018, *Astronomy & Astrophysics*, 618, A93
- Canup, R. M., & Asphaug, E. 2001, *Nature*, 412, 708
- Chatterjee, S., Ford, E. B., Matsumura, S., & Rasio, F. A. 2008, *The Astrophysical Journal*, 686, 580
- Chen, J., & Kipping, D. 2016, *The Astrophysical Journal*, 834, 17, publisher: American Astronomical Society
- Choi, J., Dotter, A., Conroy, C., et al. 2016, *ApJ*, 823, 102
- Ciardi, D. R., Crossfield, I. J. M., Feinstein, A. D., et al. 2018, *The Astronomical Journal*, 155, 10
- Claret, A. 2017, *Astronomy & Astrophysics*, 600, A30, arXiv: 1804.10295
- Collins, K. A., Kielkopf, J. F., Stassun, K. G., & Hessman, F. V. 2017, *The Astronomical Journal*, 153, 77
- Cropper, M., Katz, D., Sartoretti, P., et al. 2018, *A&A*, 616, A5
- Curtis, J. L., Agüeros, M. A., Douglas, S. T., & Meibom, S. 2019a, *The Astrophysical Journal*, 879, 49
- Curtis, J. L., Agüeros, M. A., Mamajek, E. E., Wright, J. T., & Cummings, J. D. 2019b, *The Astronomical Journal*, 158, 77
- Daban, J.-B., Gouvret, C., Guillot, T., et al. 2010, 7733, 77334T
- Damiani, F., Prisinzano, L., Pillitteri, I., Micela, G., & Sciortino, S. 2019, *Astronomy & Astrophysics*, 623, A112, publisher: EDP Sciences
- Dauphas, N., & Pourmand, A. 2011, *Nature*, 473, 489
- David, T., Hillenbrand, L., & Petigura, E. 2016, *Nature*, 534, 658
- David, T. J., & Hillenbrand, L. A. 2015, *The Astrophysical Journal*, 804, 146
- David, T. J., Petigura, E. A., Luger, R., et al. 2019a, *The Astrophysical Journal Letters*, 885, L12
- David, T. J., Mamajek, E. E., Vanderburg, A., et al. 2018, *The Astronomical Journal*, 156, 302
- David, T. J., Cody, A. M., Hedges, C. L., et al. 2019b, *The Astronomical Journal*, 158, 79
- de Zeeuw, P. T., Hoogerwerf, R., de Bruijne, J. H. J., Brown, A. G. A., & Blaauw, A. 1999, *The Astronomical Journal*, 117, 354
- Dobbie, P. D., Lodieu, N., & Sharp, R. G. 2010, *Monthly Notices of the Royal Astronomical Society*, 409, 1002
- Donati, J. F., Moutou, C., Malo, L., et al. 2016, *Nature*, advance online publication
- Dotter, A. 2016, *ApJS*, 222, 8
- Douglas, S. T., Agüeros, M. A., Covey, K. R., & Kraus, A. 2017, *The Astrophysical Journal*, 842, 83
- Douglas, S. T., Curtis, J. L., Agüeros, M. A., et al. 2019, *The Astrophysical Journal*, 879, 100
- Dullemond, C. P., & Monnier, J. D. 2010, *Annual Review of Astronomy and Astrophysics*, 48, 205
- Díaz, R. F., Almenara, J. M., Santerne, A., et al. 2014, *Monthly Notices of the Royal Astronomical Society*, 441, 983
- Ekström, S., Georgy, C., Eggenberger, P., et al. 2012, *Astronomy and Astrophysics*, 537, A146
- Elliott, P., Bayo, A., Melo, C. H. F., et al. 2016, *A&A*, 590, A13
- Evans, D. W., Riello, M., De Angeli, F., et al. 2018, *A&A*, 616, A4
- Fabrycky, D., & Tremaine, S. 2007, *The Astrophysical Journal*, 669, 1298
- Flagg, L., Johns-Krull, C. M., Nofi, L., et al. 2019, *ApJ*, 878, L37
- Foreman-Mackey, D. 2016, *The Journal of Open Source Software*, 24
- Foreman-Mackey, D., Czekala, I., Luger, R., et al. 2020, exoplanet-dev/exoplanet v0.2.6
- Fortney, J. J., Marley, M. S., & Barnes, J. W. 2007, *ApJ*, 659, 1661
- Fulton, B. J., Petigura, E. A., Blunt, S., & Sinukoff, E. 2018, *PASP*, 130, 044504
- Fulton, B. J., Petigura, E. A., Howard, A. W., et al. 2017, *AJ*, 154, 109
- Gaia Collaboration, Prusti, T., de Bruijne, J. H. J., et al. 2016, *A&A*, 595, A1
- Gaia Collaboration, Brown, A. G. A., Vallenari, A., et al. 2018, *A&A*, 616, A1
- Gaudi, B. S., & Winn, J. N. 2007, *The Astrophysical Journal*, 655, 550
- Gelman, A., & Rubin, D. B. 1992, *Statistical Science*, 7, 457, publisher: Institute of Mathematical Statistics
- Giacalone, S., & Dressing, C. D. 2020, *arXiv e-prints*, arXiv:2002.00691
- Gilbert, J., Bergmann, C., Bloxham, G., et al. 2018, 0702, 107020Y, conference Name: Ground-based and Airborne Instrumentation for Astronomy VII ISBN: 9781510619579 Place: eprint: arXiv:1807.01938
- Ginsburg, A., Sipocz, B., Madhura Parikh, et al. 2018, Astropy/Astroquery: V0.3.7 Release
- Girardi, L., Groenewegen, M. A. T., Hatziminaoglou, E., & da Costa, L. 2005, *Astronomy and Astrophysics*, 436, 895
- Hartman, J. D., Gaudi, B. S., Holman, M. J., et al. 2009, *The Astrophysical Journal*, 695, 336
- Hippke, M., David, T. J., Mulders, G. D., & Heller, R. 2019, arXiv:1906.00966 [astro-ph], arXiv: 1906.00966
- Hirano, T., Krishnamurthy, V., Gaidos, E., et al. 2020, arXiv:2006.13243 [astro-ph], arXiv: 2006.13243
- Hoffman, M. D., & Gelman, A. 2014, *Journal of Machine Learning Research*, 15, 1593
- Howard, A. W., Marcy, G. W., Bryson, S. T., et al. 2012, *The Astrophysical Journal Supplement Series*, 201, 15
- Howell, S. B., Sobeck, C., Haas, M., et al. 2014, *PASP*, 126, 398
- Huang, C. X., Burt, J., Vanderburg, A., et al. 2018, *ApJ*, 868, L39

- Hunter, J. D. 2007, *Computing in Science & Engineering*, 9, 90
- Irwin, J., & Bouvier, J. 2009, *in* , eprint: arXiv:0901.3342, 363
- Irwin, J., Irwin, M., Aigrain, S., et al. 2007, *Monthly Notices of the Royal Astronomical Society*, 375, 1449
- Jenkins, J. M., Twicken, J. D., McCauliff, S., et al. 2016, *Software and Cyberinfrastructure for Astronomy IV*, 9913, 99133E
- Johns-Krull, C. M., McLane, J. N., Prato, L., et al. 2016, *The Astrophysical Journal*, 826, 206
- Jones, E., Oliphant, T., Peterson, P., et al. 2001, Open source scientific tools for Python
- Kaufer, A., Stahl, O., Tubbings, S., et al. 1999, *The Messenger*, 95, 8
- Kharchenko, N. V., Piskunov, A. E., Röser, S., Schilbach, E., & Scholz, R.-D. 2005, *Astronomy and Astrophysics*, 438, 1163
- Kharchenko, N. V., Piskunov, A. E., Schilbach, E., Röser, S., & Scholz, R.-D. 2013, *Astronomy and Astrophysics*, 558, A53
- Kipping, D. M. 2013, *MNRAS*, 435, 2152
- Kleine, T., Touboul, M., Bourdon, B., et al. 2009, *Geochimica et Cosmochimica Acta*, 73, 5150
- Kounkel, M., & Covey, K. 2019, *The Astronomical Journal*, 158, 122
- Krumholz, M. R., McKee, C. F., & Bland-Hawthorn, J. 2019, *Annual Review of Astronomy and Astrophysics*, 57, 227
- Kurucz, R. L. 2013, *Astrophysics Source Code Library*, ascl:1303.024
- König, S., Munker, C., Hohl, S., et al. 2011, *Geochimica et Cosmochimica Acta*, 75, 2119
- Lada, C. J., & Lada, E. A. 2003, *Annual Review of Astronomy and Astrophysics*, 41, 57
- Lightkurve Collaboration, Cardoso, J. V. d. M., Hedges, C., et al. 2018, Lightkurve: Kepler and TESS time series analysis in Python, *Astrophysics Source Code Library*, ascl:1812.013
- Lin, D. N. C., Bodenheimer, P., & Richardson, D. C. 1996, *Nature*, 380, 606
- Lindgren, L., Hernández, J., Bombrun, A., et al. 2018, *Astronomy & Astrophysics*, 616, A2
- Lithwick, Y., & Wu, Y. 2014, *Proceedings of the National Academy of Sciences*, 111, 12610
- Livingston, J. H., Dai, F., Hirano, T., et al. 2018, *The Astronomical Journal*, 155, 115
- . 2019, *Monthly Notices of the Royal Astronomical Society*, 484, 8
- Lomb, N. R. 1976, *Astrophysics and Space Science*, 39, 447
- Lovis, C., & Mayor, M. 2007, *Astronomy and Astrophysics*, 472, 657
- Luger, R., Agol, E., Foreman-Mackey, D., et al. 2019, *AJ*, 157, 64
- Malavolta, L., Nascimbeni, V., Piotto, G., et al. 2016, *Astronomy and Astrophysics*, 588, A118
- Mamajek, E. E. 2009, 1158, 3, conference Name: Exoplanets and Disks: Their Formation and Diversity Place: eprint: arXiv:0906.5011
- Mamajek, E. E., & Hillenbrand, L. A. 2008, *The Astrophysical Journal*, 687, 1264
- Mann, A. W., Gaidos, E., Mace, G. N., et al. 2016a, *ApJ*, 818
- Mann, A. W., Newton, E. R., Rizzuto, A. C., et al. 2016b, *AJ*, 152, 61
- Mann, A. W., Gaidos, E., Vanderburg, A., et al. 2017, *AJ*, 153, 64
- Mann, A. W., Vanderburg, A., Rizzuto, A. C., et al. 2018, *The Astronomical Journal*, 155, 4
- Mann, A. W., Johnson, M. C., Vanderburg, A., et al. 2020, arXiv:2005.00047 [astro-ph], arXiv: 2005.00047
- Mansfield, M., Bean, J. L., Oklopčić, A., et al. 2018, *The Astrophysical Journal*, 868, L34, arXiv: 1812.02214
- Martoli, E., Hebrard, G., Moutou, C., et al. 2020, arXiv:2006.13269 [astro-ph], arXiv: 2006.13269
- Mayor, M., Marmier, M., Lovis, C., et al. 2011, *ArXiv e-prints*, 1109, arXiv:1109.2497
- McKinney, W. 2010, in *Proceedings of the 9th Python in Science Conference*, ed. S. van der Walt & J. Millman, 51
- Meibom, S., Barnes, S. A., Platais, I., et al. 2015, *Nature*, 517, 589
- Meibom, S., Torres, G., Fressin, F., et al. 2013, *Nature*, 499, 55
- Mermilliod, J. C. 1981, *Astronomy and Astrophysics*, 97, 235
- Miller, A. A., Irwin, J., Aigrain, S., Hodgkin, S., & Hebb, L. 2008, *Monthly Notices of the Royal Astronomical Society*, 387, 349
- Mochejska, B. J., Stanek, K. Z., Sasselov, D. D., et al. 2005, *The Astronomical Journal*, 129, 2856
- . 2006, *The Astronomical Journal*, 131, 1090
- Montet, B. T., Feinstein, A. D., Luger, R., et al. 2019, arXiv:1912.03794 [astro-ph], arXiv: 1912.03794
- Morton, T. D. 2012, *The Astrophysical Journal*, 761, 6
- Morton, T. D. 2015a, isochrones: Stellar model grid package
- . 2015b, VESPA: False positive probabilities calculator, *Astrophysics Source Code Library*, ascl:1503.011
- Morton, T. D., Bryson, S. T., Coughlin, J. L., et al. 2016, *The Astrophysical Journal*, 822, 86, arXiv: 1605.02825
- Netopil, M., Paunzen, E., Heiter, U., & Soubiran, C. 2016, *Astronomy and Astrophysics*, 585, A150
- Newton, E. R., Mann, A. W., Tofflemire, B. M., et al. 2019, *The Astrophysical Journal*, 880, L17
- Obermeier, C., Henning, T., Schlieder, J. E., et al. 2016, *The Astronomical Journal*, 152, 223
- Oh, S., Price-Whelan, A. M., Hogg, D. W., Morton, T. D., & Spergel, D. N. 2017, *The Astronomical Journal*, 153, 257
- Oklopčić, A., & Hirata, C. M. 2018, *ApJL*, 855, L11
- Owen, J. E., & Wu, Y. 2013, *ApJ*, 775, 105
- Palle, E., Oshagh, M., Casasayas-Barris, N., et al. 2020, arXiv:2006.13609 [astro-ph], arXiv: 2006.13609
- Paxton, B., Bildsten, L., Dotter, A., et al. 2011, *ApJS*, 192, 3

- Paxton, B., Cantiello, M., Arras, P., et al. 2013, *ApJS*, **208**, 4
- Paxton, B., Marchant, P., Schwab, J., et al. 2015, *ApJS*, **220**, 15
- Pepper, J., Stanek, K. Z., Pogge, R. W., et al. 2008, *The Astronomical Journal*, **135**, 907
- Pérez, F., & Granger, B. E. 2007, *Computing in Science and Engineering*, **9**, 21
- Petigura, E. A., Marcy, G. W., Winn, J. N., et al. 2018, *The Astronomical Journal*, **155**, 89
- Plavchan, P., Barclay, T., Gagné, J., et al. 2020, *Nature*, **582**, 497, arXiv: 2006.13248
- Pollack, J. B., Hubickyj, O., Bodenheimer, P., et al. 1996, *Icarus*, **124**, 62
- Quinn, S. N., White, R. J., Latham, D. W., et al. 2012, *ApJ Letters*, **756**, L33
- Raghavan, D., McAlister, H. A., Henry, T. J., et al. 2010, *The Astrophysical Journal Supplement Series*, **190**, 1, arXiv: 1007.0414
- Randich, S., Tognelli, E., Jackson, R., et al. 2018, *Astronomy & Astrophysics*, **612**, A99
- Raymond, S. N., Kokubo, E., Morbidelli, A., Morishima, R., & Walsh, K. J. 2014, *Protostars and Planets VI*, 595
- Rebull, L. M., Stauffer, J. R., Cody, A. M., et al. 2020
- Rebull, L. M., Stauffer, J. R., Bouvier, J., et al. 2016, *The Astronomical Journal*, **152**, 113
- Ricker, G. R., Winn, J. N., Vanderspek, R., et al. 2015, *Journal of Astronomical Telescopes, Instruments, and Systems*, **1**, 014003
- Rizzuto, A. C., Vanderburg, A., Mann, A. W., et al. 2018, arXiv:1808.07068 [astro-ph], arXiv: 1808.07068
- Rizzuto, A. C., Newton, E. R., Mann, A. W., et al. 2020, arXiv:2005.00013 [astro-ph], arXiv: 2005.00013
- Rohatgi, A. 2019, WebPlotDigitizer: v4.2
- Salvatier, J., Wiecki, T. V., & Fonnesbeck, C. 2016, PyMC3: Python probabilistic programming framework
- Santerne, A., Díaz, R. F., Almenara, J.-M., et al. 2015, *MNRAS*, **451**, 2337
- Sato, B., Izumiura, H., Toyota, E., et al. 2007, *ApJ*, **661**, 527
- Scargle, J. D. 1982, *ApJ*, **263**, 835
- Seager, S., & Mallén-Ornelas, G. 2003, *ApJ*, **585**, 1038
- Servén, D., Brummitt, C., & Abedi, H. 2018, dswah/pyGAM: v0.8.0
- Skrutskie, M. F., Cutri, R. M., Stiening, R., et al. 2006, *The Astronomical Journal*, **131**, 1163
- Skumanich, A. 1972, *The Astrophysical Journal*, **171**, 565
- Smith, J. C., Morris, R. L., Jenkins, J. M., et al. 2016, *PASP*, **128**, 124501
- Smith, J. C., Stumpe, M. C., Cleve, J. E. V., et al. 2012, *PASP*, **124**, 1000
- Soderblom, D. R. 2010, *Annual Review of Astronomy and Astrophysics*, **48**, 581
- Soderblom, D. R., Hillenbrand, L. A., Jeffries, R. D., Mamajek, E. E., & Naylor, T. 2014, *Protostars and Planets VI*, 219
- Spake, J. J., Sing, D. K., Evans, T. M., et al. 2018, *Nature*, **557**, 68, arXiv: 1805.01298
- Stassun, K. G., Collins, K. A., & Gaudi, B. S. 2017, *The Astronomical Journal*, **153**, 136
- Stassun, K. G., Oelkers, R. J., Pepper, J., et al. 2018, *AJ*, **156**, 102
- Stassun, K. G., Oelkers, R. J., Paegert, M., et al. 2019, arXiv:1905.10694 [astro-ph], arXiv: 1905.10694
- Stauffer, J. R., Hartmann, L. W., Prosser, C. F., et al. 1997, *The Astrophysical Journal*, **479**, 776
- Stumpe, M. C., Smith, J. C., Catanzarite, J. H., et al. 2014, *PASP*, **126**, 100
- Sullivan, P. W., et al. 2015, *ApJ*, **809**, 77
- Theano Development Team. 2016, arXiv e-prints, abs/1605.02688
- Tokovinin, A. 2018, *Publications of the Astronomical Society of the Pacific*, **130**, 035002, arXiv: 1801.04772
- Tokovinin, A., Fischer, D. A., Bonati, M., et al. 2013, *Publications of the Astronomical Society of the Pacific*, **125**, 1336
- Torres, G., Fressin, F., Batalha, N. M., et al. 2011, *The Astrophysical Journal*, **727**, 24
- van Leeuwen, F. 2009, *Astronomy and Astrophysics*, **497**, 209
- Vanderburg, A., Mann, A. W., Rizzuto, A., et al. 2018, arXiv:1805.11117 [astro-ph], arXiv: 1805.11117
- Vanderburg, A., Huang, C. X., Rodriguez, J. E., et al. 2019, *The Astrophysical Journal*, **881**, L19
- VanderPlas, J. T., & Ivezić, Z. 2015, *ApJ*, **812**, 18
- Walt, S. v. d., Colbert, S. C., & Varoquaux, G. 2011, *Computing in Science & Engineering*, **13**, 22
- Weber, E. J., & Davis, Jr., L. 1967, *The Astrophysical Journal*, **148**, 217
- Williams, J. P., & Cieza, L. A. 2011, *Annual Review of Astronomy and Astrophysics*, **49**, 67
- Wright, E. L., Eisenhardt, P. R. M., Mainzer, A. K., et al. 2010, *The Astronomical Journal*, **140**, 1868
- Wright, J. T., Marcy, G. W., Howard, A. W., et al. 2012, *The Astrophysical Journal*, **753**, 160
- Zahn, J.-P. 1977, *Astronomy and Astrophysics*, **500**, 121
- Zhou, G., Winn, J. N., Newton, E. R., et al. 2019, arXiv:1912.04095 [astro-ph], arXiv: 1912.04095
- Ziegler, C., Tokovinin, A., Briceño, C., et al. 2020, *AJ*, **159**, 19
- Zuckerman, B., & Song, I. 2004, *Annual Review of Astronomy and Astrophysics*, **42**, 685
- Žerjal, M., Zwitter, T., Matijević, G., et al. 2017, *The Astrophysical Journal*, **835**, 61
- Žerjal, M., Ireland, M. J., Nordlander, T., et al. 2019, *Monthly Notices of the Royal Astronomical Society*, **484**, 4591, arXiv: 1810.10435